Journal of Colloid and Interface Science 654 (2024) 1378–1392

Contents lists available at ScienceDirect

Journal of Colloid And Interface Science

journal homepage: www.elsevier.com/locate/jcis

CeO_2 nanorods supported CuO_x-RuO_x bimetallic catalysts for low temperature CO oxidation

Md Robayet Ahasan, Ruigang Wang *

Department of Metallurgical and Materials Engineering, The University of Alabama, Tuscaloosa, AL 35487, United States

GRAPHICAL ABSTRACT

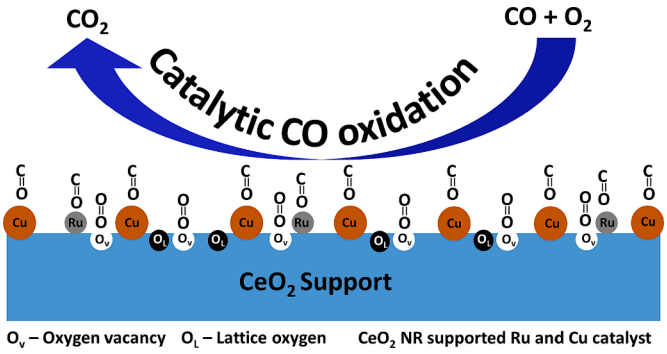

ARTICLE INFO

Keywords:
In situ DRIFTS
CO-TPD
CuO_x-RuO_x bimetallic catalyst
CeO_2 nanorods
CO oxidation

ABSTRACT

Bimetallic catalysts often outperform monometallic catalysts due to changeable structural orientation, synergistic effects, and integration of two different metal or metal oxide properties. Here, a series of CeO_2 nanorods (NR) supported bimetallic CuO_x and RuO_x catalysts (Cu: Ru ratios of 9:1, 7:3, and 5:5) were prepared using a wet impregnation method. *In situ* DRIFTS, H_2 temperature programmed reduction (H_2-TPR), CO temperature programmed desorption (CO-TPD), and other characterization techniques were used to investigate the effect of the Cu:Ru ratio on the activity of low-temperature CO oxidation. Among three catalysts, CeO_2 NR supported 7 wt% Cu-3 wt% Ru catalyst after a reduction activation treatment showed the best performance with 100 % CO conversion at 166 °C and the lowest activation energy of 18.37 kJ mol^{-1}. Raman and XPS profiles revealed that the origin of the superior performance is at least partially related to the high surface oxygen vacancy concentration and other distinct oxygen species (physi-/chemi-sorbed oxygen and bulk lattice oxygen), leading to outstanding adsorption and oxidation property of CO.

1. Introduction

CO oxidation via heterogeneous gas–solid catalysis is prominent due to its impressive activity, selectivity, and resistance toward catalyst deactivation, as well as its low energy consumption and environmentally friendly process [1,2]. More recently, it has become increasingly

* Corresponding author.
E-mail address: rwang@eng.ua.edu (R. Wang).

https://doi.org/10.1016/j.jcis.2023.10.113
Received 29 July 2023; Received in revised form 30 September 2023; Accepted 21 October 2023
Available online 24 October 2023

apparent that surface engineered ceria (CeO_2) as a support can significantly promote the activity of supported metal or metal oxide catalysts for low temperature CO oxidation thanks to the strong metal support interaction (SMSI) and/or oxygen exchange. CeO_2 is frequently prescribed as a catalyst promoter due to its facile oxygen mobility (oxygen release and storage capacity), easy oxygen vacancy formation, and remarkable redox property (easy transition between Ce^{4+} and Ce^{3+}) due to the narrow Ce f-band [3]. In addition, shape-controlled or surface engineered CeO_2 nanoparticles, such as nanorods (NR), nanocubes (NC), and nanofibers (NF), showed distinct catalytic activity due to the superiority in cluster trapping/anchoring, tuning of exposed crystal planes, and SMSI [4–6]. Face centered cubic CeO_2 has three most thermodynamically stable crystal planes: (1 1 1), (1 1 0), and (1 0 0) [7]. The surface energy and oxygen vacancy formation energy follow the order (1 1 1) < (1 1 0) < (1 0 0) and (1 1 0) < (1 0 0) < (1 1 1), respectively [8]. High resolution transmission electron microscopy (HRTEM) studies have shown that CeO_2 NR exposed the majority of (1 1 0) and (1 0 0) facets, while defect-rich (1 1 1) planes were also observed [9,10]. For example, Pan et al. [11] studied the effect of CeO_2 shapes on the CO oxidation performance using CeO_2 NR, nanowires (NW), nanotubes (NT), and NC. They concluded that CeO_2 NR exhibited enhanced low temperature catalytic properties due to the exposed (1 1 0) facets. Likewise, Lin et al. [12] reported that Au/CeO_2 NR presented superior water–gas-shift performance compared to Au/CeO_2 NC. In the same vein, Wang et al. [13] reported excellent CO oxidation performance for cost-effective transitional metal doped CeO_2 NR.

Noble metals Pt, Pd, Au, and Rh are well-known active catalysts for low temperature "oxidation" reactions due to their high catalytic activity [14]. Recently, CeO_2 supported Ru has been frequently reported to present outstanding lower temperature CO oxidation activity [15,16]. For instance, Mitsui et al. [17] showed that Ru-based CeO_2 catalysts excelled over other noble metals Pt, Pd, and Rh-based CeO_2 catalysts for the oxidation of ethyl acetate. Ru is known to be able to facilitate the breakdown of C—C and C—H bonds [18]. In addition, the addition of Ru in CeO_2 enhances oxygen vacancy formation and promotes both chemisorption and weak physisorption of CO molecules [19]. It was also reported that the Ru^{4+} ion substitution in the CeO_2 lattice can activate the oxygen supply during oxidation and play a crucial role in low-temperature CO oxidation. Besides CO oxidation, Ru-incorporated CeO_2 was also reported as highly active catalyst for CO_2 methanation and alcohol or aldehyde oxidation [20].

On the other side, recently, transitional metal oxides have attracted significant attention to replace noble metals as cost-effective and sustainable alternative catalysts for CO oxidation. Among a variety of transition metal oxides, the Cu-based catalysts (Cu–Cu_2O–CuO system) showed remarkable performance on low-temperature CO oxidation, which was well reported from both theoretical and experimental aspects [21,22]. For example, Guo et al. [23] claimed that CuO/CeO_2-rod and CuO/CeO_2-polyhedra have higher low-temperature catalytic oxidation due to highly active species of Cu^+, more vital interaction with CeO_2 support, and more oxygen vacancies on the surface. It was noted that Cu ions prefer to oxidize as Cu^+ with the exposure of (1 1 1) plane of CeO_2, which was also considered as a key factor of higher catalytic activity on shape controlled CeO_2 [24]. Martinez et al. [25] reported that CuO_x ($0 \leq x \leq 1$) clusters can be partially or fully reduced with CeO_2 and provide Cu^+ species for CO chemisorption. At the same step, oxygen can be supplied by CeO_2 support by the Ce^{4+}/Ce^{3+} redox cycle, which provides oxygen species for the CO oxidation reaction.

Bimetallic catalysts and metal alloys have emerged as a popular material design approach to improve catalytic activity compared to its monometallic catalyst counterpart. For example, Guo et al. [26] reported that the addition of a secondary metal Mn, in Cu-based catalyst, reduced the half CO conversion (T_{50}) temperature from 371.3-455 K to 369.6-389.2 K. Pt-Ru bimetallic catalysts have also been investigated for their effective synergy in electrooxidation of methanol or direct methanol fuel cell (DMFC) [27]. Many experimental and theoretical studies highlighted the critical role of the interfaces between bimetallic catalyst clusters with supporting material [28,29]. In this study, we intend to investigate the performance of CeO_2 NR supported CuO_x-RuO_x (x is a variable due to the catalyst-support interaction and oxidation/reduction treatments) bimetallic catalysts for low-temperature CO oxidation. While previous studies have extensively examined Cu and Ru-based CeO_2 monometallic catalysts for CO oxidation, limited experimental evidence exists for CuO_x-RuO_x bimetallic catalysts' interaction with CeO_2. Therefore, the present study seeks to investigate the synergy between CuO_x and RuO_x on the CeO_2 support for CO oxidation.

2. Experimental

2.1. Catalyst preparation

CeO_2 NR support was prepared by a hydrothermal method consistent with our previous investigation [30,31]. Here, 8 mL of 6.0 M NaOH (VWR, 99 %) solution was mixed dropwise with 88 mL of 0.1 M Ce $(NO_3)_3 \cdot 6H_2O$ (Acros Organics, 99.5 %) solution in a 200 mL Teflon liner and stirred for ~15 s. Then the white precipitated suspension was put into a stainless-steel autoclave with tight sealing and heated at a ramping temperature of 10 °C/min and kept at 90 °C for 48 h. Following the hydrothermal reaction, the sample went through a filtering process by thoroughly washing with distilled water and ethanol, respectively, to remove the residual salts and to avoid hard agglomeration of the nanoparticles. The collected sample was then dried at 60 °C for 12 h and grinded with mortar and pestle to obtain CeO_2 NR powder.

The incipient wet impregnation method was used to prepare the CeO_2 NR supported CuO_x-RuO_x bimetallic catalysts. First, each 0.9 g CeO_2 NR was suspended in three 200 mL beakers with 100 mL deionized water. Then, $Cu(NO_3)_2 \cdot 2.5H_2O$ and $Ru(NO)(NO_3)_3$ (Alfa Aesar) were added based on the Cu and Ru ratios of 9:1, 7:3 and 5:5, followed by tuning the pH value of the solution with 0.5 M aqueous solution of ammonium hydroxide ($NH_3 \cdot H_2O$, BDH, 28–30 vol%) to ~9. The suspensions were then stirred (400 rpm) for 4 h at 80 °C and dried in an oven overnight. After that, the dried powders were calcined at 350 °C for 5 h (the oxidized sample, i.e., 9 wt% Cu-1 wt% Ru/CeO_2 NR-o). Afterwards, a portion of each of the oxidized samples was reduced in a tube furnace under 5 vol% H_2-95 vol% He atmosphere at 300 °C for 5 h (the reduced sample, i.e., 9 wt% Cu-1 wt% Ru/CeO_2 NR-r).

2.2. Catalyst characterization

The powder samples were analyzed using a Phillips X'Pert MPD diffractometer for X-ray diffraction (XRD) equipped with a copper Kα radiation source with a wavelength (λ) of 0.154 nm, voltage of 40 kV, and emission current of 40 mA. The diffraction pattern was recorded with a step size of 0.5° min^{-1} in the range of 2θ between 10 °C and 90 °C. JADE software was utilized for XRD pattern analysis and phase identification.

Surface area was assessed using a single point Brunauer-Emmett-Teller (BET) method with nitrogen physisorption at ~77 K. H_2-temperature programmed reduction (H_2-TPR) was carried out using a Micromeritics AutoChem II 2920 chemisorption analyzer. The sample (85–95 mg) was placed in a quartz U-tube with quartz wool and heated at a ramp rate of 10 °C/min from 30 °C to 900 °C. Concurrently, a 10 vol % H_2– 90 vol% Ar gas mixture with a 50 mL/min flow rate was supplied. A thermal conductivity detector (TCD) was used to measure the H_2 uptake during the reaction.

Carbon monoxide temperature-programmed desorption, or CO-TPD, was used to examine the interaction of CO with the catalyst surface. This characterization was performed using the same chemisorption analyzer (Micromeritics AutoChem II 2920). Each powder sample was first placed put in a quartz U-tube microreactor sandwiched with quartz wool. Then the sample was heated from room temperature to 400 °C in He stream (flow rate: 50 mL/min) to eliminate residual moisture. After the sample

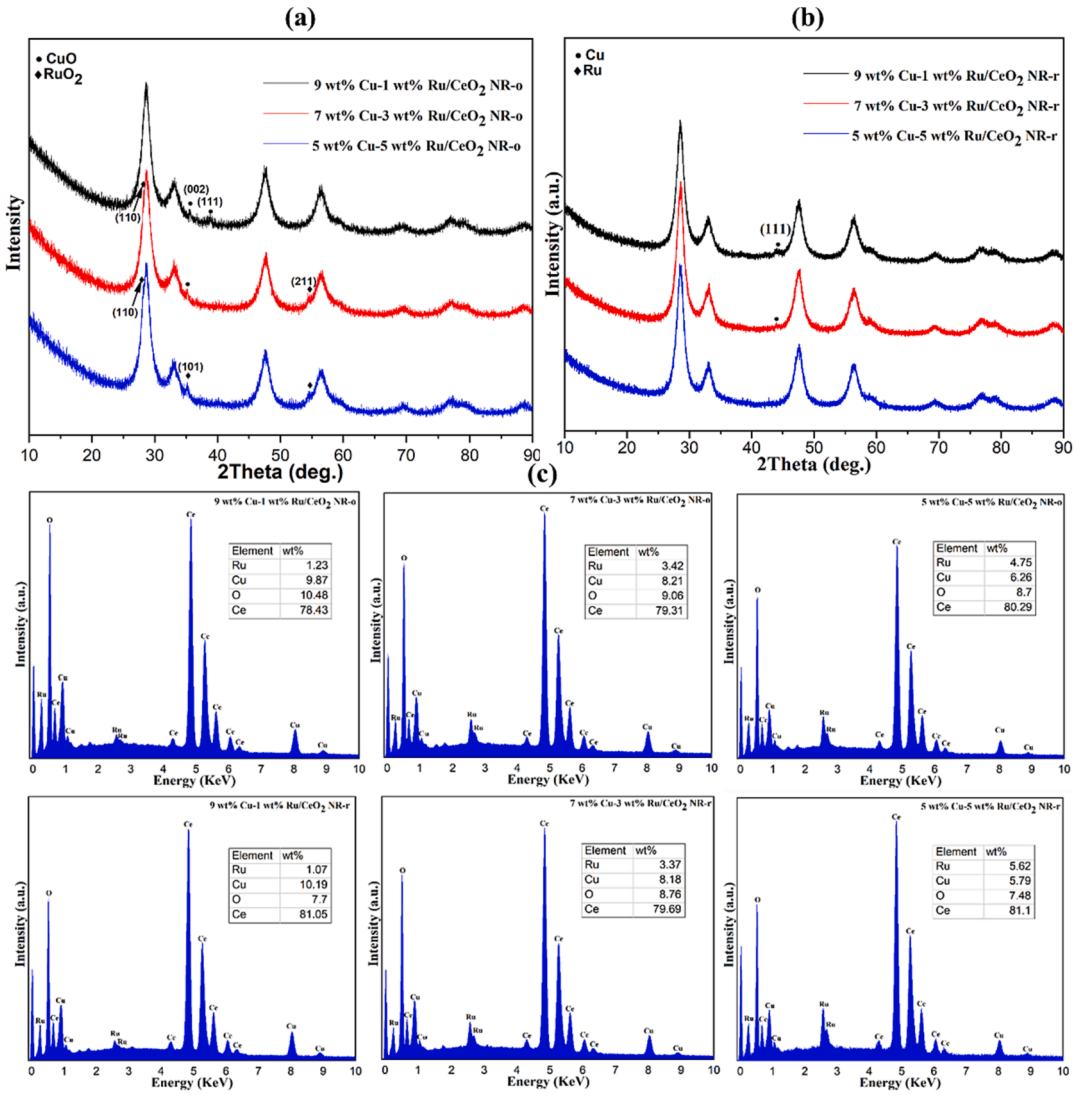

Fig. 1. (a, b) XRD patterns (a: the oxidized samples and b: the reduced samples) and (c) EDS line profiles of CeO_2 NR supported CuO_x-RuO_x bimetallic catalysts before and after the reduction treatment.

was cooled down to room temperature, 10 vol% CO-90 vol% He mixture gas flowed at 50 mL/min through the sample for 60 min. Finally, under He gas environment, the CO desorption behavior of the catalyst was subsequently recorded using a TCD by ramping the temperature up to 800 °C at a linear heating rate of 10 °C/min.

The sample for TEM characterization was prepared using diluted powder suspension with ethanol which was dropped on a 400-mesh copper grid (Ted Pella Inc.) following ultrasonication and was then dried in air. HRTEM and TEM images for the prepared samples were taken by a FEI Tecnai F20 TEM with an acceleration voltage of 200 kV to analyze particle size, morphology, and atomic-level structure. A JEOL 7000 FE SEM instrument was used to obtain energy-dispersive X-ray spectra (EDS) and elemental mappings.

For Raman spectroscopy characterization, a Horiba LabRAM HR 800 Raman spectrometer (equipped with 100x-long working distance objective, NA = 0.60) was used to assess each catalyst in the spectral window of 100 to 1200 cm^{-1}. Prior to analysis, a diode-pumped solid-state (DPSS) laser system (Laser Quantum MPC6000) tuned at λ = 532 nm was used for excitation. Before executing each analysis, the spectrometer was calibrated via a single crystal Si wafer.

A Kratos Axis Ultra DLD spectrometer was used for X-ray photoelectron spectroscopy (XPS) analysis to determine the elemental chemical states and surface composition. The data was collected by using a monochromatic Al Kα (hv = 1486.6 eV) source under ultra-high vacuum (10^{-10} Torr), and the binding energies were calibrated internally by the carbon deposit C 1s binding energy (BE) at 284.8 eV. The CASA XPS software was used to conduct the fitting and deconvolution of the profiles.

Temperature and time dependent *in situ* diffuse reflectance infrared Fourier transform spectroscopy (DRIFTS) experiments were measured by a Nicolet 6700 Fourier-transform infrared (FTIR) spectrometer equipped with a Harrick Praying Mantis DRIFTS accessory, with a resolution of 4 cm^{-1}. For CO adsorption, 1 vol% CO and 99 vol% Ar gas mixture was fed into the reactor with a flow rate of 100 mL/min for 20 or 35 min. Prior to each CO adsorption step, the sample was pretreated with Ar gas with a flow rate of 100 mL/min at 200 °C for 30 min to remove moisture.

2.3. Catalytic activity measurements

The catalytic performance of the prepared samples was carried out by CO oxidation in a downward fixed bed glass tubular reactor. 30 mg of each sample was put into a glass tube with quartz wool and directly exposed to a gas mixture of 1 vol% CO, 20 vol% O_2, and 79 vol% He at a flow rate of 38 mL/min with a corresponding weight hour space velocity (WHSV) value of 76,000 mL h^{-1} g_{cat}^{-1}, without any pretreatment. The

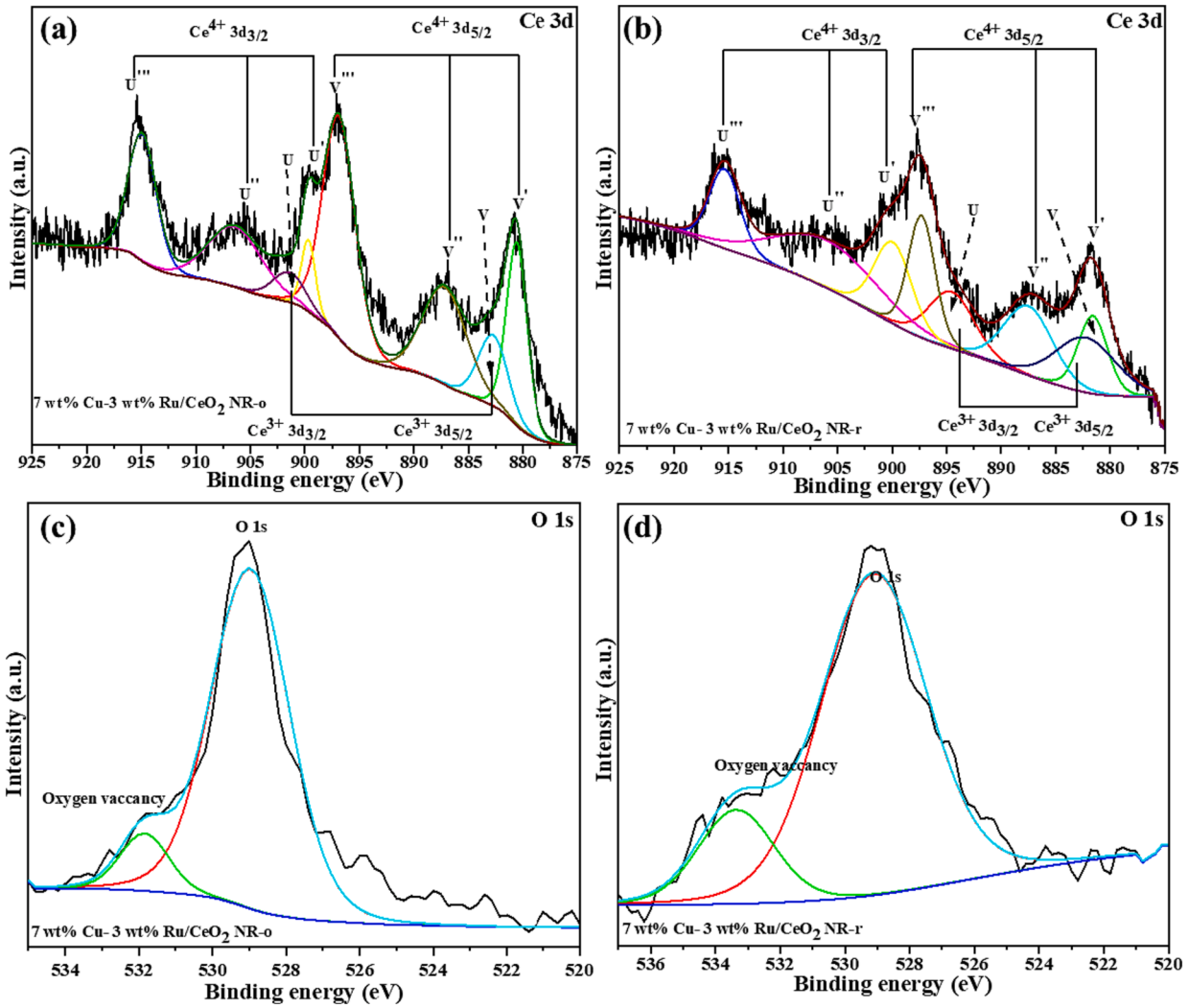

Fig. 2. XPS spectra of (a, b) Ce 3d and (c, d) O 1s of the oxidized (a and c) and reduced (b and d) CeO_2 NR supported 7 wt% Cu-3 wt% Ru catalysts.

reactor temperature was programmed from room temperature to 400 °C. An online gas chromatograph (SRI multiple gas analyzer GC, chassis) was used to measure the concentration of CO and CO_2. The following equation was used to calculate the CO conversion:

$$\text{CO conversion}\,(\%) = \frac{[CO]_{inlet} - [CO]_{outlet}}{[CO]_{inlet}} * 100\% \quad (1)$$

Here, $[CO]_{inlet}$ is the input concentration of CO gas, and $[CO]_{outlet}$ is the output concentration of CO gas.

3. Result and discussion

3.1. XRD analysis

Fig. 1 **(a, b)** display the XRD profiles of three CuO_x-RuO_x bimetallic samples after the oxidation (Fig. 1 **(a)**) and reduction (Fig. 1 **(b)**) treatments. In addition, Fig. 1 **(c)** depicts the compositional analysis using EDS for each sample, which confirms the Cu/Ru ratios of the prepared catalysts. The XRD data in Fig. 1 **(a, b)** mainly exhibit the face-centered cubic fluorite CeO_2 structure. According to the JCPDS database (#34-0394), the observed peaks at 28.6°, 33.1°, 47.6°, 56.3° correspond to the (111), (200), (220) and (311) planes of CeO_2 structure, respectively. From Fig. 1 **(a)**, the diffraction pattern of the 9 wt% Cu-1 wt% Ru/CeO_2 NR-o sample shows two diffraction peaks at 35.5° and 38.9° in addition to those of CeO_2, referring to the (002) and (111) planes of CuO_x, respectively. For 7 wt% Cu-3 wt% Ru/CeO_2 NR-o, CuO_x and RuO_x phases appear at 35.2 ° and 54.6°, representing (002) and (211) planes, respectively. Finally, for 5 wt% Cu-5 wt% Ru/CeO_2 NR-o, the CuO_x phases "disappear", while the (101) and (211) planes of RuO_x can be observed. In comparison, the XRD data for the reduced samples in Fig. 1 **(b)** do not reveal any peaks for RuO_x while depicting a weak Cu peak corresponding to the (111) plane for the 9 wt% Cu-1 wt% Ru/CeO_2 NR and 7 wt% Cu-3 wt% Ru/CeO_2 NR catalysts. This lack of RuO_x peaks is largely due to the formation of Ru-O-Ce solid solution and/or small particle size of RuO_x [32]. Despite this, EDS line spectra in Fig. 1 **(c)** clearly showed the presence of Ru, verifying its concentration which is nearly equal to the designed Cu-Ru composition ratio.

3.2. XPS analysis

XPS was used to investigate the chemical oxidation states of Ce, Ru, Cu, and O species on the surface of the catalysts. As shown in Figs. 2 and 3, the deconvoluted XPS spectra of Ce 3d, O 1s, Ru 3d, and Cu 2p were extracted from the survey for both oxidized and reduced 7 wt% Cu-3 wt % Ru/CeO_2 NR catalysts. Fig. 2 **(a, b)** compare the Ce 3d profiles of the 7 wt% Cu-3 wt% Ru/CeO_2 NR-o and 7 wt% Cu-3 wt% Ru/CeO_2 NR-r catalysts. The letters U and V are denoted to $3d_{3/2}$ and $3d_{5/2}$ final states, respectively. The peaks recorded at 915.5, 906.4, 900.1, 897.5, 886.4, and 881.4 eV are addressed by U‴, U″, U′, V‴, V″, and V′, respectively, corresponding to the Ce^{4+} state, the primary cerium

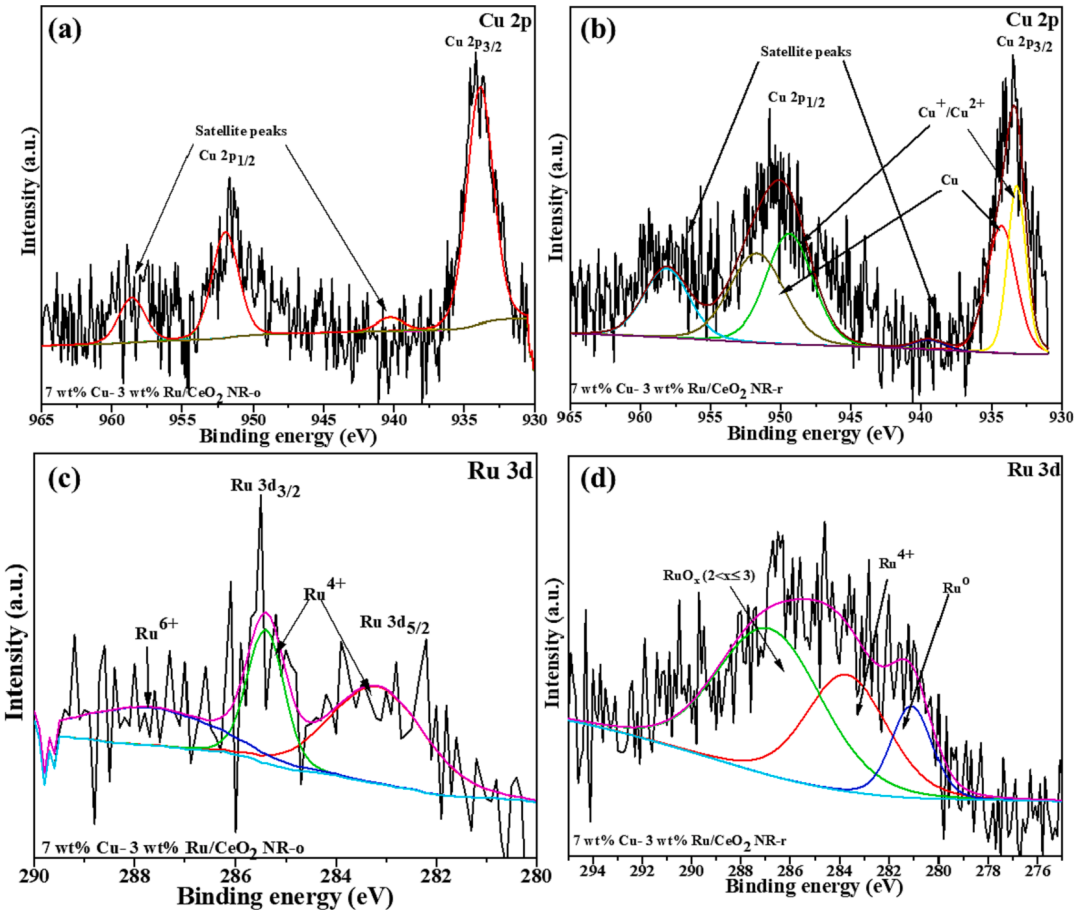

Fig. 3. XPS spectra of (a, b) Cu 2P and (c, d) Ru 3d of the oxidized (a and c) and reduced (b and d) CeO_2 NR supported 7 wt% Cu-3 wt% Ru catalysts.

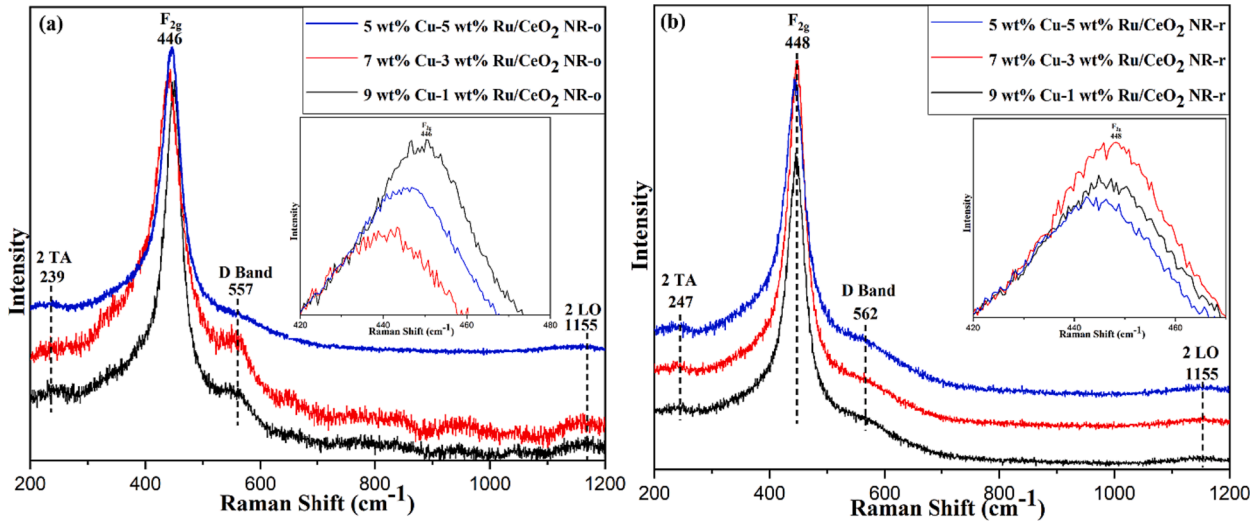

Fig. 4. Raman spectroscopy characterization of CeO_2 NR supported CuO_x-RuO_x bimetallic catalysts before (a: the oxidized samples) and after the reduction treatment (b: the reduced samples).

valence state of CeO_{2-x} [33]. In contrast, the peaks U and V at 895.2 and 881.7 eV are assigned to the Ce^{3+} state. The Ce^{3+} concentration in the 7 wt% Cu-3 wt% Ru/CeO_2 NR-r catalyst is higher than that in the 7 wt% Cu-3 wt% Ru/CeO_2 NR-o catalyst. Therefore, it can be reasonably concluded that the reduction treatment resulted in a higher concentration of oxygen vacancy and Ce^{3+}. This conclusion is validated with the O 1s spectra, as shown in Fig. 2 **(c, d)**. The peaks were fitted using the Gaussian function at B.E. = 529.1 eV and 532.4 eV assigned for $[O]^{4+}_{Ce}$ and $[O]^{3+}_{Ce}$ oxygen bounds, respectively [34]. The oxygen-bound peaks for Ce^{3+} for the 7 wt% Cu-3 wt% Ru/CeO_2 NR-r catalyst are greater than in the 7 wt% Cu-3 wt% Ru/CeO_2 NR-o catalyst, indicating the presence of large amount of oxygen vacancies. According to Mars-van Krevelen theory, surface oxygen species of CeO_2 supported metal or metal oxide catalysts play a key role in chemically adsorption of CO. Because CO first

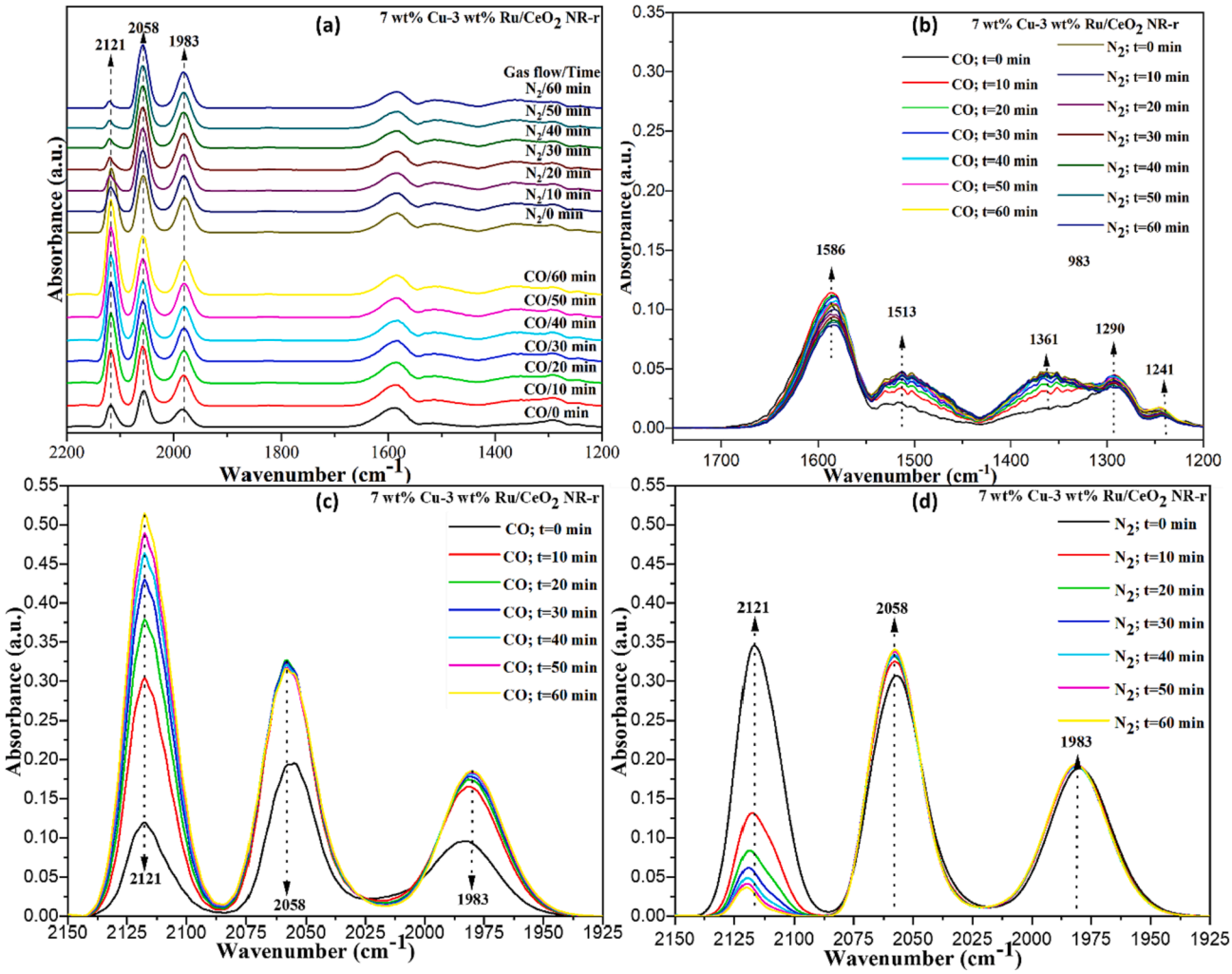

Fig. 5. Time-dependent *in situ* DRIFTS spectra of CO adsorption on the 7 wt% Cu-3 wt% Ru/CeO_2 NR-r catalyst.

interacts with (i.e., adsorbs on) active sites over CeO_2 supported catalysts, followed by the migration of the adsorbed CO species to the metal-support interface. Meanwhile, the CO species can react with oxygen on the surface of the support and form oxygen vacancy. Subsequently, the process will then proceed with the replacement of the oxygen vacancies by gas-phase oxygen migration [35,36].

Fig. 3 **(a, b)** shows the XPS profiles of Cu 2p for the oxidized and reduced CeO_2 NR supported 7 wt% Cu-3 wt% Ru catalysts, presenting two main peaks at 933.1 and 953.1 eV, which belong to the Cu $2P_{3/2}$ and Cu $2P_{1/2}$, respectively. The 20 eV separation between these two peaks confirms the existence of CuO in the oxidized catalyst. The satellite peaks also exist in the Cu 2p XPS spectra. After the reduction treatment, the core peak Cu $2P_{3/2}$ of the reduced sample can be fitted into two components at 935.5 and 954.5 eV, indicating metallic Cu and the mixture of Cu^{2+}/Cu^{+} ions based on their binding energy. It is worth mentioning that it is challenging to distinguish Cu^{2+} and Cu^{+} ions thanks to the close binding energies. The XPS spectra confirm the existence of Ce^{4+}/Ce^{3+}, Cu^{2+}/Cu^{+}, and oxygen vacancies, suggesting a strong interaction between well-dispersed copper oxide species and CeO_2 NR enriched with surface defects through $Ce^{4+} + Cu^{+} \leftrightarrow Ce^{3+} + Cu^{2+}$ during the redox treatments. The deconvolution of the Ru 3d core level spectra in Fig. 3 **(c, d)** demonstrates the existence of multiple oxidation states of Ru. However, after the reduction treatment, there is an undefined oxidation state of Ru^{n+} $(4 < n < 6)$, suggesting a possible diffusion of Ru into CeO_2 lattice or replacement of Ce^{4+} site with Ru ions, leading to the formation of Ru-O-Ce solid solution. This observation is consistent with the results from other characterization techniques. For instance, due to the Ru doping, the H_2 TPR profiles show an improved low-temperature reducibility of CeO_2 and the XRD profiles for the CeO_2 supported catalysts shift a little due to the different ionic sizes of Ru and Ce. The Ru^{n+} $(4 < n < 6)/Ru^{4+}$-rich surface is more favorable for CO catalytic oxidation at lower temperatures than $Ru^{n+}(4 < n < 6)/Ru^{6+}$-rich surface. This is because Ru^{n+} diffuse into CeO_2 lattice and create Ru-O-Ce solid solution via electron transfer interface, leading to a higher amount of oxygen vacancy.

3.3. Raman spectroscopy analysis

Raman spectroscopy is a favorable structural characterization technique owing to the study of the defects of CeO_2 and for investigating the interaction between active metal or metal oxide clusters and CeO_2 support. Raman spectroscopy analysis was employed on the oxidized and reduced CeO_2 NR supported CuO_x-RuO_x with the Cu/Ru ratios of 9:1, 7:3, and 5:5, as illustrated in Fig. 4 **(a, b)**. The recorded peaks at 239, 446, 557, and 1155 cm^{-1} correspond to the second-order transverse acoustic mode (2TA), the F_{2g} mode of fluorite phase, the defect-induced mode (D mode), and the second-order longitudinal optical mode (2LO band) of CeO_2, respectively [37].

In Fig. 4 **(a)**, the intensity of the Raman spectra associated with CeO_2 NR at 446 cm^{-1} decreases in the following order for the oxidized samples: 7 wt% Cu-3 wt% Ru/CeO_2 NR > 5 wt% Cu-5 wt% Ru/CeO_2 NR > 9 wt% Cu-1 wt% Ru/CeO_2 NR. In addition, the peak at 557 cm^{-1}

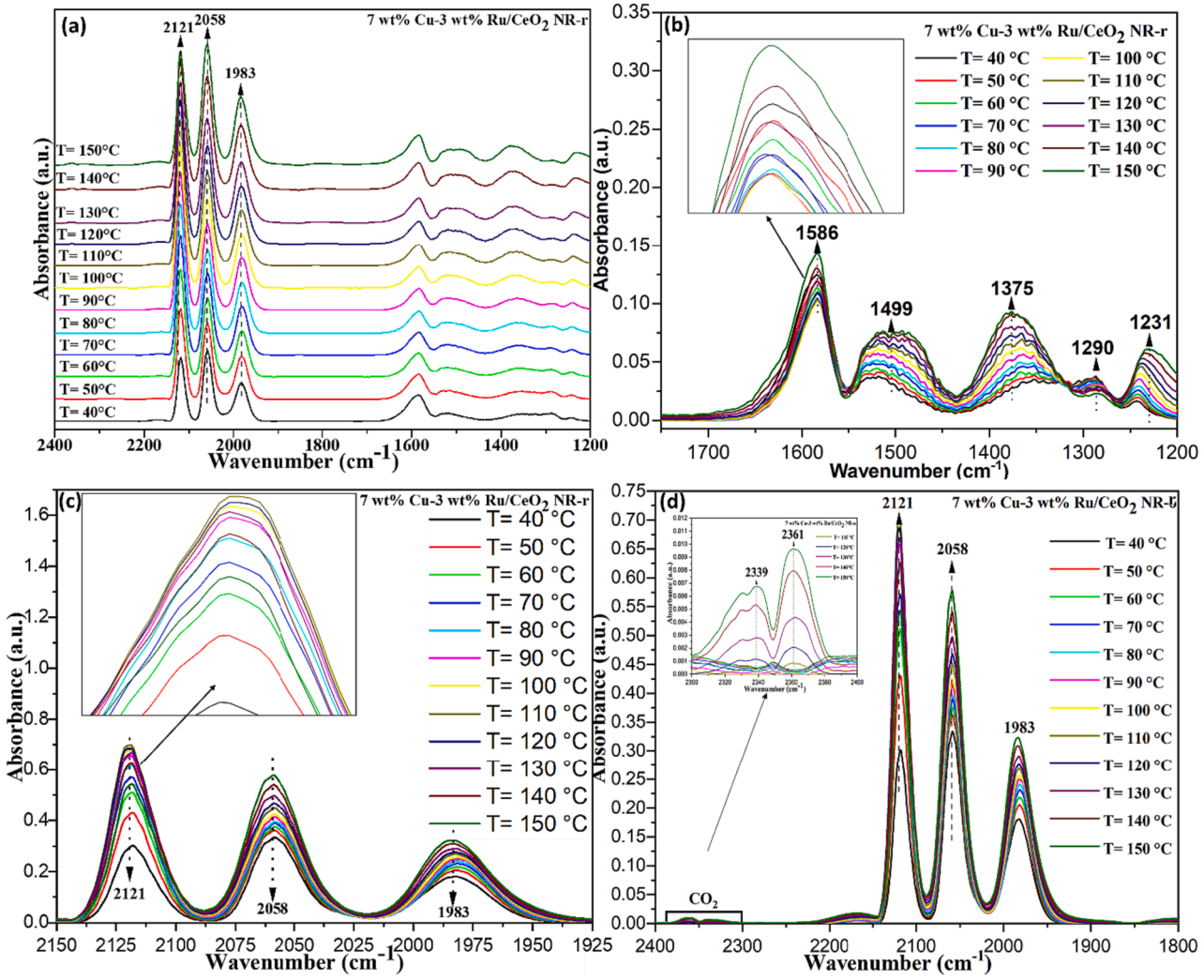

Fig. 6. Temperature-dependent *in situ* DRIFTS spectra of CO adsorption on the 7 wt% Cu-3 wt% Ru/CeO_2 NR-r catalyst.

Table 1
Vibration frequencies and bond assignments of adsorbed or formed species over the 7 wt% Cu-3 wt% Ru/CeO_2 NR-r catalyst.

Species	Bond types	Frequency (cm^{-1})	References
		7 wt% Cu-3 wt% Ru/CeO_2 NR-r	
Adsorbed CO	Ru-CO	2058	[39,41,45,47–49]
Surface oxo species	Polydentate carbonate	1586	
	Mono dentate carbonate	1513	
	Formates	1361	
	Bi or tri carbonates	1241, 1290	

corresponds to oxygen vacancies, showing a substantial increased intensity in the CeO_2 NR supported 7 wt% Cu-3 wt% Ru catalyst compared to the other two samples. This observation suggests that the optimal Cu to Ru ratio of 7:3 fosters increased CeO_2 defects and higher oxygen vacancy concentration. The higher concentration of oxygen vacancies can be resulted from the incorporation of Cu^{2+}/Cu^{+} and $Ru^{\delta+}$ species into the CeO_2 lattice. Moreover, it is notable that the F_{2g} peak shifts to a lower wavenumber for the CeO_2 NR supported 7 wt% Cu-3 wt% Ru sample, implying a degradation of CeO_2 symmetry and lattice distortion due to the synergy of CuO_x and RuO_x [38]. In contrast, the reduced samples display the opposite trend in Fig. 4 **(b)**. The CeO_2 NR supported 7 wt% Cu-3 wt% Ru sample exhibit a higher F_{2g} peak intensity than the CeO_2 NR supported 5 wt% Cu-5 wt% Ru/ and 9 wt% Cu-1 wt% Ru samples. Also, the F_{2g} peak for the reduced samples undergoes a blue shift compared to the oxidized samples, indicating better crystallinity in all reduced samples. According to the literature, the A_g, B_{1g}, B_{2u}, and B_{2g} modes for CuO were observed at 271, 326, 506, and 625 cm^{-1}, respectively, while the corresponding values for Ru species are 655 and 975 cm^{-1}. In our case, no apparent peaks corresponding to CuO_x and RuO_x were seen, indicating a SMSI and/or the formation of Cu–O-Ce and Ru-O-Ce solid solutions. The Raman spectra reveal that the 7 wt% Cu-3 wt% Ru/CeO_2 NR-r sample has a greater number of lattice defects and oxygen vacancies which can promote CO oxidation more prominently than other samples.

3.4. *In situ* DRIFTS analysis

Fig. 5 **(a)** shows the time-dependent *in situ* DRIFTS spectra of CO adsorption at 35 °C on the 7 wt% Cu-3 wt% Ru/CeO_2 NR-r catalyst. The bands between 1800 cm^{-1} to 2300 cm^{-1} reflect the adsorbed gaseous CO, whereas the bands between 1200 cm^{-1} to 1800 cm^{-1} represent CO adsorption on the catalyst surface, forming various weak surface species [39]. In time-dependent *in situ* DRIFTS characterization, a 1 vol% CO/N_2 flow was used for the first 60 min to achieve complete coverage of CO molecules at the surface adsorption site. During CO flow, CO gas phase

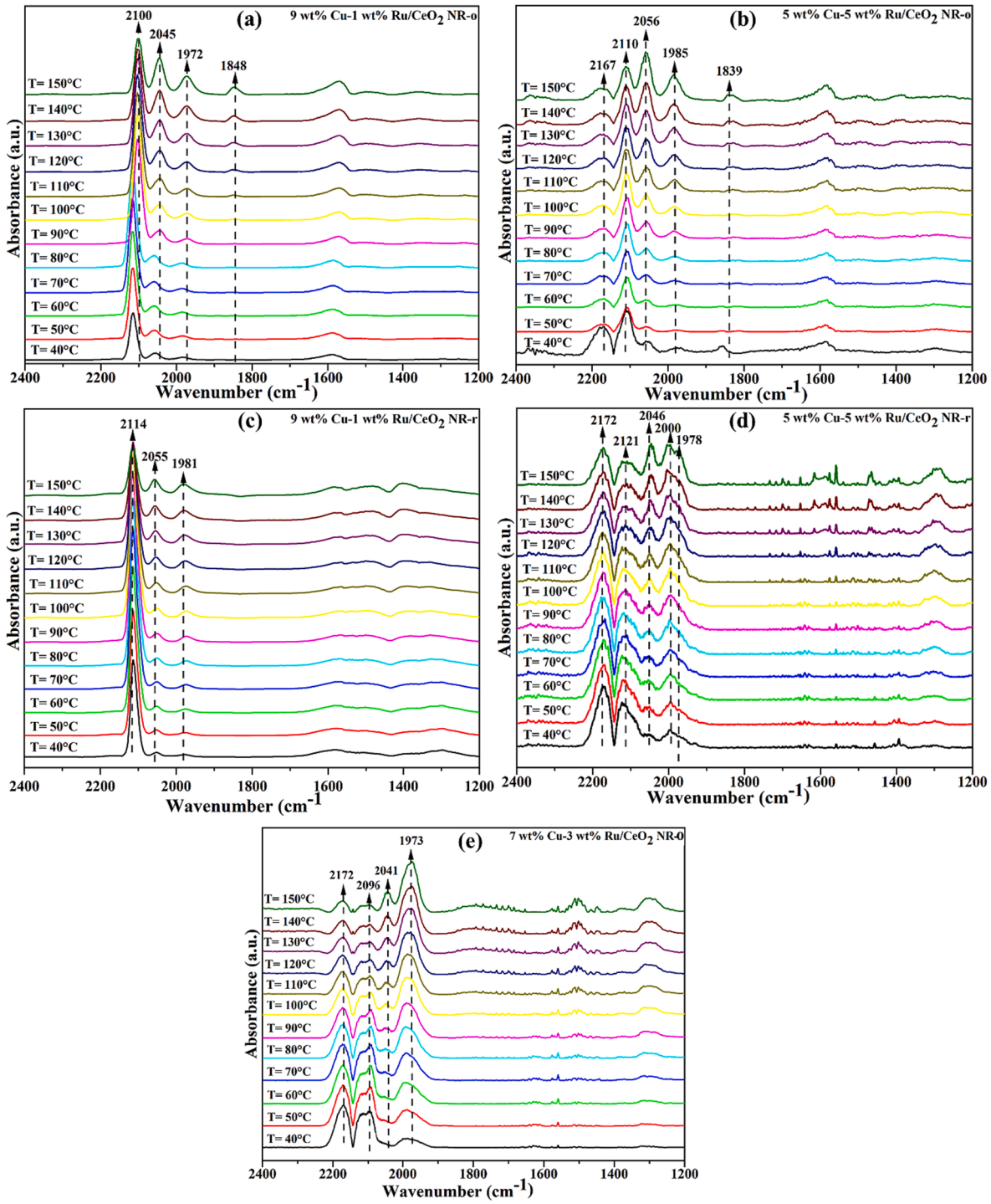

Fig. 7. Temperature-dependent *in situ* DRIFTS spectra of CO adsorption on CeO_2 NR supported CuO_x-RuO_x bimetallic catalysts before and after the reduction treatment.

bands at 2121 cm^{-1}, 2058 $cm^{-1,}$ and 1983 cm^{-1} were identified. Subsequently, a 60-minute flow of N_2 gas was initiated to remove ambient CO and weakly adsorbed CO species. The band identified at 2121 cm^{-1} in Fig. 5 **(c, d)** is attributed to free gaseous CO in the chamber because the intensity of this band nearly disappears over time during N_2 gas flow. However, the bands at 2058 cm^{-1} and 1983 cm^{-1} remain unchanged when N_2 replaces CO. The band at 2058 cm^{-1} was assigned to multicarbonyl species by binding CO molecules with $Ru^{\delta+}$ [8,40]. Based on the literature, the band identified at 1983 cm^{-1} in Fig. 5 **(a, c, and d)** is still unclear. However, according to Xu et al. [41], this band represents the multicarbonyl CO species adsorbed on Ru^o or partially reduced Ru. Several research articles linked this band to CO adsorption on Ru-doped CeO_2 [42–44].

Fig. 5 **(b)** shows several bands at 1586 cm^{-1}, 1513 cm^{-1}, 1361 cm^{-1}, 1290 cm^{-1}, and 1241 cm^{-1}. These bands represent the most intense vibrational modes of surface species formed by CO adsorption, such as carbonates, formats, or bidentates. Because CO molecules, acting as electron donor probes, can be trapped by oxygen. According to the literature, surface oxo species are often referred to as "surface poisoning" for catalysts because they can block the catalyst's surface and

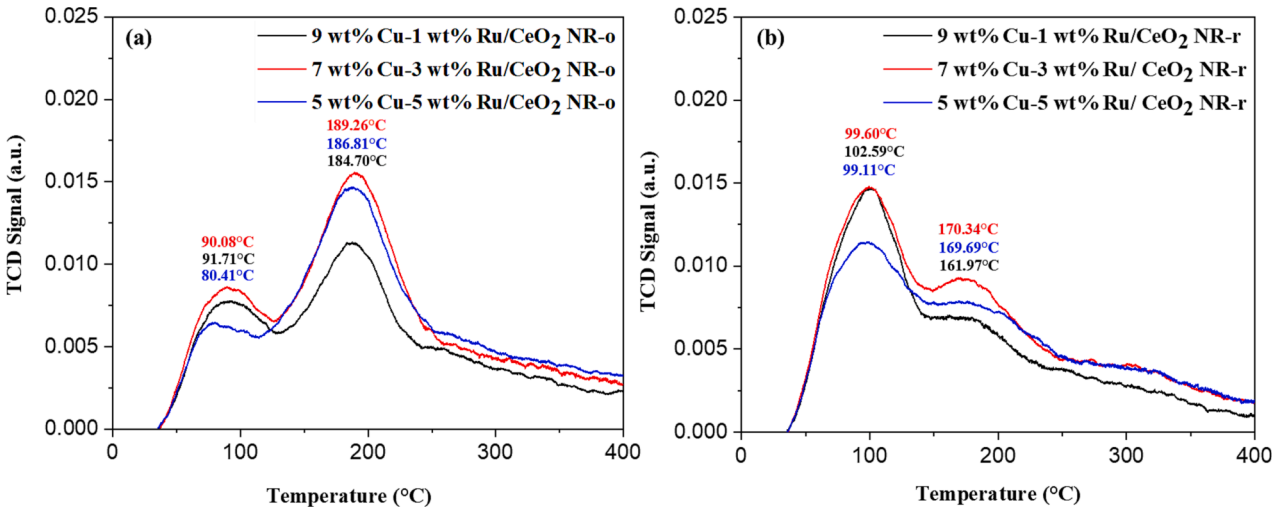

Fig. 8. CO-TPD of CeO_2 NR supported CuO_x-RuO_x bimetallic catalysts before (a: the oxidized samples) and after the reduction treatment (b: the reduced samples).

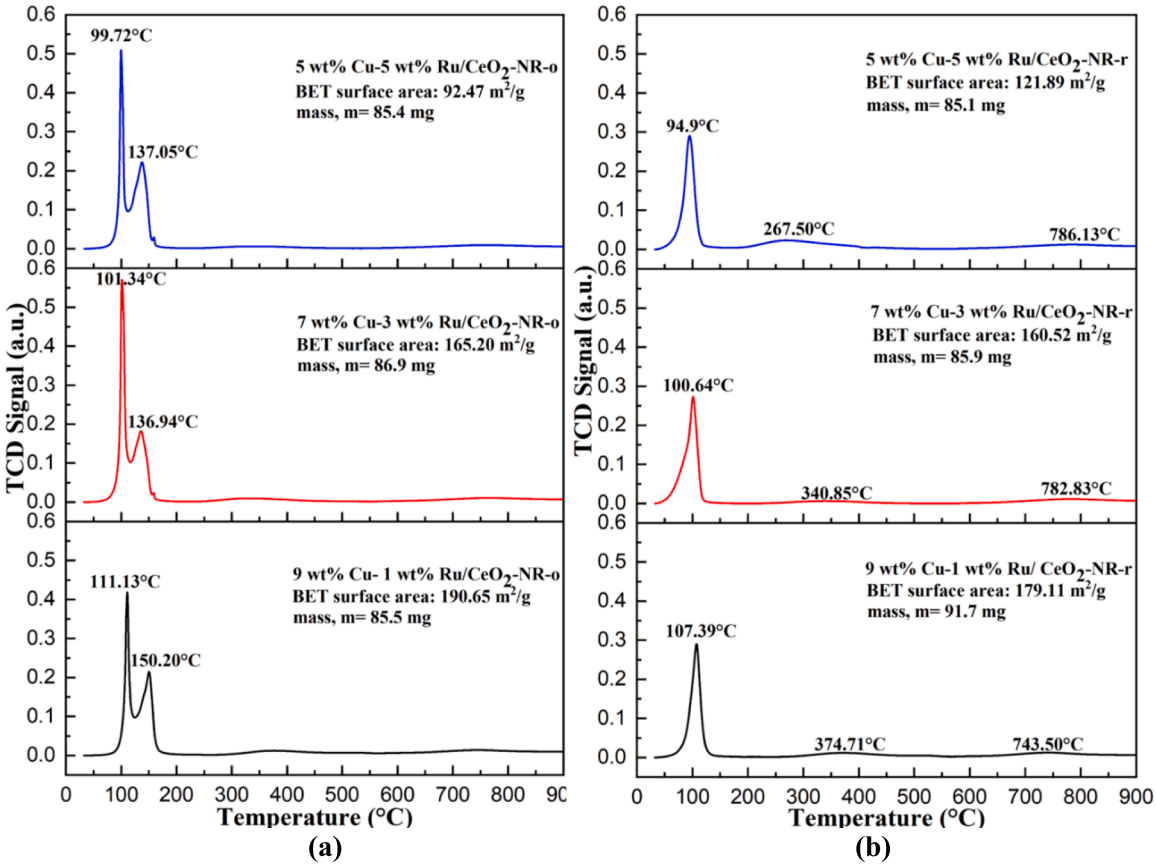

Fig. 9. H_2-TPR profiles of (a) the oxidized CeO_2 NR supported bimetallic CuO_x-RuO_x catalysts and (b) the reduced CeO_2 NR supported bimetallic CuO_x-RuO_x catalysts.

limit the CO conversion rate [45]. However, as shown in Fig. 5 **(a) and** Fig. 6 **(a)**, these surface species tend to diminish gradually with time (during both CO and N_2 flow) and temperature (until 110 °C) [46] (see Table 1).

Fig. 6 presents the temperature-dependent *in situ* DRIFTS spectra of the 7 wt% Cu-3 wt% Ru/CeO_2 NR-r catalyst from 40 °C to 150 °C. In Fig. 6 **(a, d)**, the bands appeared at 2339 cm^{-1} and 2361 cm^{-1} correspond to the formation of CO_2. Referring to Fig. 6 **(d)**, these two CO_2 bands emerged at 120 °C, and at the same temperature, associating with a decrease in CO uptake. This consistency is due to the conversion of CO to CO_2 at 120 °C or greater, which is closer to CO_2 formation energy [8].

Fig. 7 **(a-e)** depict the temperature-dependent *in situ* DRIFTS spectra of CO adsorption on 9 wt% Cu-1 wt% Ru/CeO_2 NR-o, 5 wt% Cu-5 wt% Ru/CeO_2 NR-o, 9 wt% Cu-1 wt% Ru/CeO_2 NR-r, 5 wt% Cu-5 wt% Ru/CeO_2 NR-r and 7 wt% Cu-3 wt% Ru/CeO_2 NR-o samples from the temperatures ranging from 40 °C to 150 °C. As mentioned previously, the CO *in situ* DRIFTS spectra for these catalysts exhibit a peak arrangement of gaseous CO adsorption in 2200 cm^{-1} to 1800 cm^{-1} region, with

Table 2
H_2 consumption and reduction temperature of the prepared samples from the H_2-TPR profiles.

S/N	Sample	H_2 consumption (μmol/g)			Initial reduction temperature (°C)
		Surface reduction by Ru	Surface reduction by Cu	Total surface reduction	
1	9 wt% Cu-1 wt% Ru/CeO_2 NR-o	1238.05	1158.66	2396.71	59
2	7 wt% Cu-3 wt% Ru/CeO_2 NR-o	1675.71	1282.72	2958.43	57
3	5 wt% Cu-5 wt% Ru/CeO_2 NR-o	1303.07	1624.88	2927.95	61
4	9 wt% Cu-1 wt% Ru/CeO_2 NR-r	N/A	N/A	1515.91	42
5	7 wt% Cu-3 wt% Ru/CeO_2 NR-r	N/A	N/A	1852.39	36
6	5 wt% Cu-5 wt% Ru/CeO_2 NR-r	N/A	N/A	1836.04	43

surface products in the range of 1800 cm^{-1} to 1200 cm^{-1}.

3.5. CO-TPD

The CO-TPD is broadly used to evaluate the surface-active sites and gas adsorption strength of a catalyst. In a typical CO-TPD experiment, CO molecules adsorb on the catalyst's surface and ultimately desorb as CO_2 via the interaction of adsorbed CO with the surface/lattice oxygen of the catalyst [50–52]. Fig. 8 **(a, b)** illustrates the CO-TPD profiles of the oxidized and reduced CeO_2 NR supported CuO_x-RuO_x bimetallic catalysts. All the oxidized samples exhibit two distinct desorption peaks.

The peak between 80 ℃ to 90 ℃ reflects the CO_2 desorption of weakly adsorbed CO. The second peak, ranging from 180 ℃ to 190 ℃, is assigned to the CO_2 desorption of CO interacted with weakly adsorbed CO and/or bidentate carbonate species [53]. Based on earlier experiment [54], CeO_2 NR exhibited two desorption peaks at 130 ℃ and 600 ℃. In comparison, the desorption peak intensity is higher for the CeO_2 NR supported CuO_x-RuO_x bimetallic catalysts. This indicates that the interaction between CuO_x-RuO_x and CeO_2 NR support facilitates CO adsorption with higher amount and at lower temperatures. After reduction treatment, there are still two desorption peaks, but the relative intensity reverts. This can be attributed to the reduction of CuO_x and RuO_x to metallic Cu and Ru.

3.6. H_2-TPR and BET surface area

The reducibility of all the CeO_2 NR supported CuO_x-RuO_x bimetallic catalysts was assessed using the H_2-TPR characterization. Fig. 9 **(a, b)** illustrate the H_2-TPR profiles of the oxidized and reduced CeO_2 NR supported CuO_x-RuO_x bimetallic catalysts with the Cu: Ru ratios of 9:1,

Table 3
Catalytic performance and apparent activation energy (E_a) of various catalysts.

Samples	T_{50} (°C)	T_{100} (°C)	E_a (kj*mol^{-1})	Crystalline size (nm)
CeO_2 NR	315	–	51.52	3.92
CuO	220	–	83.10	19.2
RuO_2	181	–	39.06	5.54
9 wt% Cu-1 wt% Ru/CeO_2-NR-o	132	232	32.41	4.15
7 wt% Cu-3 wt% Ru/CeO_2-NR-o	126	187	26.59	3.89
5 wt% Cu-5 wt% Ru/CeO_2-NR-o	135	276	29.09	4.07
9 wt% Cu-1 wt% Ru/CeO_2-NR-r	94	187	24.93	5.09
7 wt% Cu-3 wt% Ru/CeO_2-NR-r	87	166	18.37	5.28
5 wt% Cu-5 wt% Ru/CeO_2-NR-r	91	200	21.61	5.17

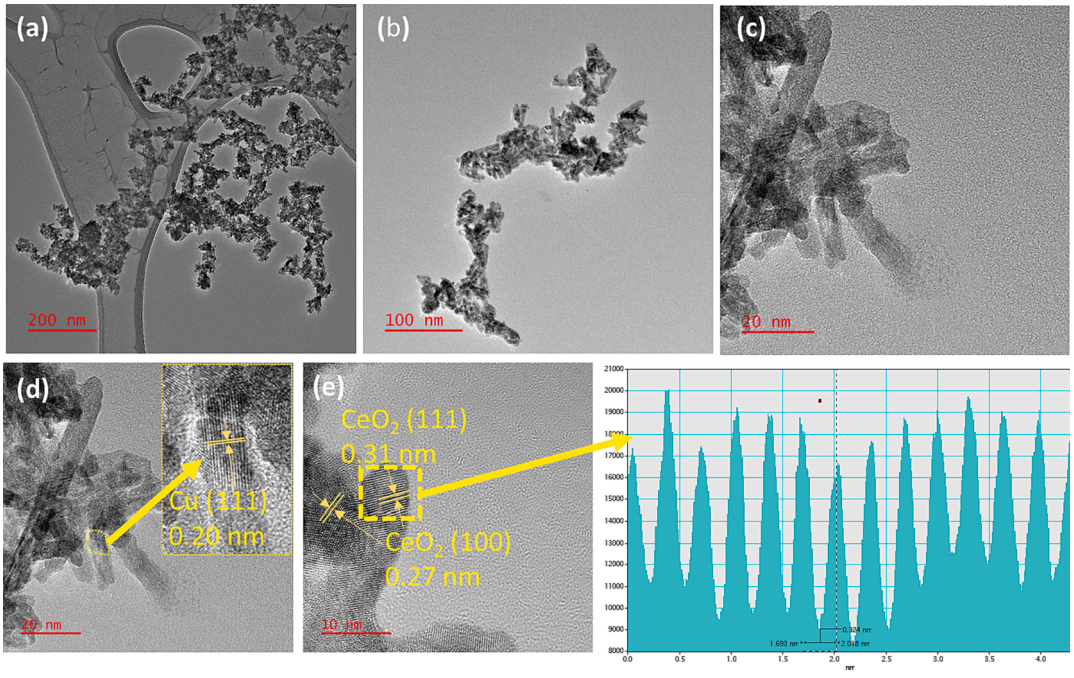

Fig. 10. TEM images of the 7 wt% Cu-1 wt% Ru/CeO_2 NR-r catalyst.

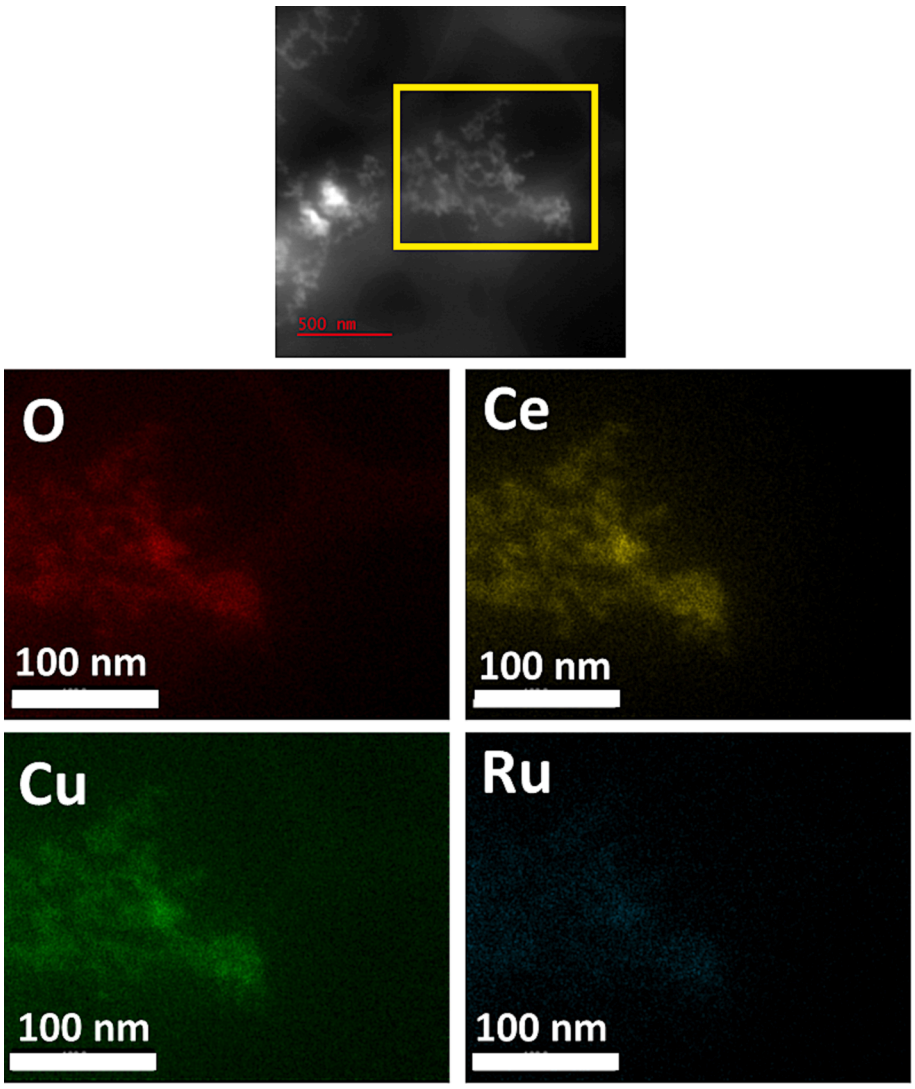

Fig. 11. EDS elemental mapping of the 7 wt% Cu-1 wt% Ru/CeO_2 NR-r catalyst.

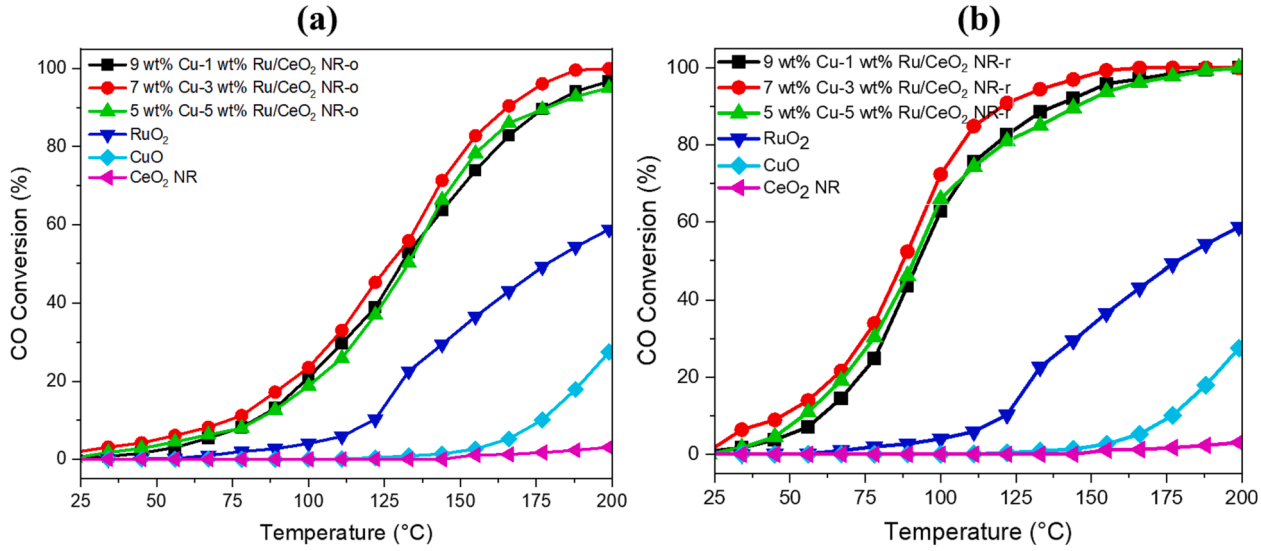

Fig. 12. CO conversion over CeO_2 NR, CuO, RuO_2, and CeO_2 NR supported CuO_x-RuO_x bimetallic catalysts before (a: the oxidized samples) and after the reduction treatment (b: the reduced samples).

Table 4
Comparison of CO oxidation activity over different catalysts.

Catalyst	Operating parameters	Temperature (100 % CO conversion)	References
5 wt% CuO-CeO_2	20 mg of catalyst with a reaction gas mixture of 1 vol% CO balanced with dry air. The total flow rate was 10 mL min^{-1} and GHSV was 30,000 mL (h g $_{cat}$)$^{-1}$	200 °C	[67]
5.2 wt% Cu/TiO_2 (oxidized)	50 mg of catalyst with a reaction gas mixture of 5 vol% CO/He balanced with dry air. The total flow rate was 50 mL min^{-1} and WHSV was 60,000 mL (h g $_{cat}$)$^{-1}$	198 °C	[68]
5 wt% CuO/CeO_2 −500	250 mg of catalyst with a reaction gas mixture of 1 vol% CO, 1 vol% O_2 balanced with N_2. The total flow rate was 40 mL min^{-1} and WHSV was 9600 mL (h g $_{cat}$)$^{-1}$	180 °C	[69]
4 wt% CuO/ZrO_2	200 mg of catalyst with a reaction gas mixture of 10 vol% CO balanced with dry air. The total flow rate was 36.6 mL min^{-1} and WHSV was 11,000 mL (h g $_{cat}$)$^{-1}$	180 °C	[70]
15 wt% Cu/$LaCoO_3$	40 mg of catalyst with a reaction gas mixture of 4 vol% CO and 2 vol% O_2 balanced with Ar. The total flow rate was 100 mL min^{-1} and WHSV was 150,000 mL (h g $_{cat}$)$^{-1}$	400 °C	[71]
$Cu_{0.1}Ce_{0.9}O_{2-x}$	20 mg of catalyst with a reaction gas mixture of 1 vol% CO and 2.5 vol% O_2 balanced with Ar. The total flow rate was 26 mL min^{-1} and WHSV was 78,000 mL (h g $_{cat}$)$^{-1}$	180 °C	[72]
7 wt% Cu-3 wt% Ru/CeO_2 NR-r	30 mg of catalyst with a reaction mixture of 1 vol % CO, 20 vol% O_2, and 79 vol% He. The total flow rate was 38 mL min^{-1} and WHSV was 76,000 mL (h g $_{cat}$)$^{-1}$	166 °C	This work

7:3, and 5:5. In Fig. 9 **(a)**, all oxidized bimetallic samples exhibit two peaks below 200 °C. The first peak ranges from 99.72 to 111.13 °C, while the second peak ranges from 136.94 to 150.20 °C. The first peak corresponds to the reduction of RuO_x, whereas the second peak corresponds to the reduction of CuO_x. Nevertheless, several scholarly studies have reported a two-step reduction profile for Cu-based catalysts using the following equation:

$$CuO \rightarrow Cu_2O \rightarrow Cu \quad (2)$$

In Eq. (2), the first reduction step belongs to the low-temperature reduction peak of CuO, representing a strong interaction of smaller and well-dispersed crystalline CuO_x with CeO_2 support. The second reduction step of Eq. (2) is ascribed to larger "bulk-like" CuO_x particles that interact weakly with CeO_2 support [55]. The strong and low-temperature reduction peaks appeared in Fig. 9 **(a)** could be associated to the simultaneous reduction of RuO_x from *RuO_2 to Ru* and CuO_x from *CuO to Cu_2O*, where a fraction of CuO_x was reduced at a lower temperature in the presence of RuO_x. The higher-temperature peak observed for all oxidized samples in Fig. 9 **(a)** is attributed to the reduction of isolated CuO_x, as represented by the second part of Eq. (2), from *Cu_2O to Cu* [56]. According to literature, the reduction temperature of CuO and RuO_2 is in the following ranges: 380 °C to 390 °C for CuO and 130 °C to 230 °C for RuO_2. While pure CeO_2 NR support typically exhibits the surface and bulk reduction peaks at ~400 °C and 750 °C, respectively [5,57,58]. Thus, it can be concluded that the noticeably improved low-temperature reductivity of the supported catalysts is due to the metal-support synergy.

The reduction profiles of all the reduced samples exhibited a "single" peak below 200 °C, suggesting lower surface H_2 consumption than the oxidized samples, within the temperature range of 94.9 to 107.4 °C. For one possible explanation, this "single" reduction peak is more likely attributed to RuO_x related phase(s), as RuO_2 is reportedly reduced to Ru between 100 and 200 °C [59]. In this study, the reduced samples were subjected to H_2 reduction at 300 °C. Hence, the other possible explanation for the "single" reduction peak below 200 °C is provided below. It is probable that all of the RuO_x was reduced to Ru, whereas only partial reduction happened for CuO_x. During the H_2-TPR characterization for the reduced samples, there was no RuO_x present for reduction, and the two-step H_2-TPR reduction profile of CuO_x (known as α and β peak) merged into a "single" peak. The merging of CuO_x peaks can be explained by a possible transformation of β-type CuO_x species to α-type CuO_x at a low reduction temperature. There are other peaks visible between 200 and 400 °C and 700 to 800 °C, which would be the possible reduction of large particle CuO_x and bulk reduction of CeO_2 support.

Table 2 presents a quantitative analysis of the H_2 consumption and reduction temperature data illustrated in Fig. 9 **(a, b)**. Each of the prepared sample showed significant surface H_2 consumption and low initial reduction temperatures. The quantitative analysis in Table 2 indicates that when the amount of Ru addition increased from 1 wt% to 3 wt%, there was a considerable increase in H_2 consumption for each catalyst along with a decrease in the initial reduction temperature. It is also important to note that all reduced samples consumed approximately one-third less H_2 than the oxidized sample and exhibited a lower reduction temperature. This can be attributed to the reduced oxygen storage capacity and the activation of the metal catalyst (i.e., RuO_x) by the reduction treatment, respectively. For example, Liu et al. [60] reported that the presence of noble metals improved the reduction characteristics of transition metal oxide. This phenomenon is known as the H_2 spillover effect [61]. Therefore, an optimum ratio of RuO_x and CuO_x composition can enhance the synergistic effect among RuO_x, CuO_x, and CeO_2 (support material).

3.7. TEM and EDX analysis

Fig. 10 **(a-e)** demonstrate that the incorporation of CuO_x and RuO_x onto CeO_2 NR does not significantly alter the morphology, size, and crystal structures of CeO_2 NR. The dimension of the reduced 7 wt% Cu-1 wt% Ru/CeO_2 catalyst nanoparticles are approximately 70 nm in length and 8 nm in diameter, which is a little larger than the value estimated from XRD (Table 3). The HRTEM images in Fig. 10 (d, e) demonstrate the exposed crystal planes of CeO_2 (1 1 1) and Cu (1 1 1) plane. Notably, the HRTEM images and line-profiles of the 7 wt% Cu-1 wt% Ru/CeO_2 NR-r catalyst demonstrate the absence of Ru, which can be attributed to the low deposition and/or strong RuO_x-CeO_2 interaction. However, the EDX analysis and elemental mapping analysis in Fig. 11 confirm the presence of Ru over the CeO_2 NR support in the 7 wt% Cu-1 wt% Ru/CeO_2 NR-r catalyst. In addition, the EDS elemental mapping shows a uniform distribution of Cu and Ru over the CeO_2 NR support. The rough surface of CeO_2 NR is another surface characteristic seen in the HRTEM images (Fig. 10), along with lattice distortion, lattice flaws, and voids.

3.8. CO oxidation

The catalytic performance of CeO_2 NR-supported CuO_x-RuO_x bimetallic catalysts was assessed using CO oxidation as a model reaction.

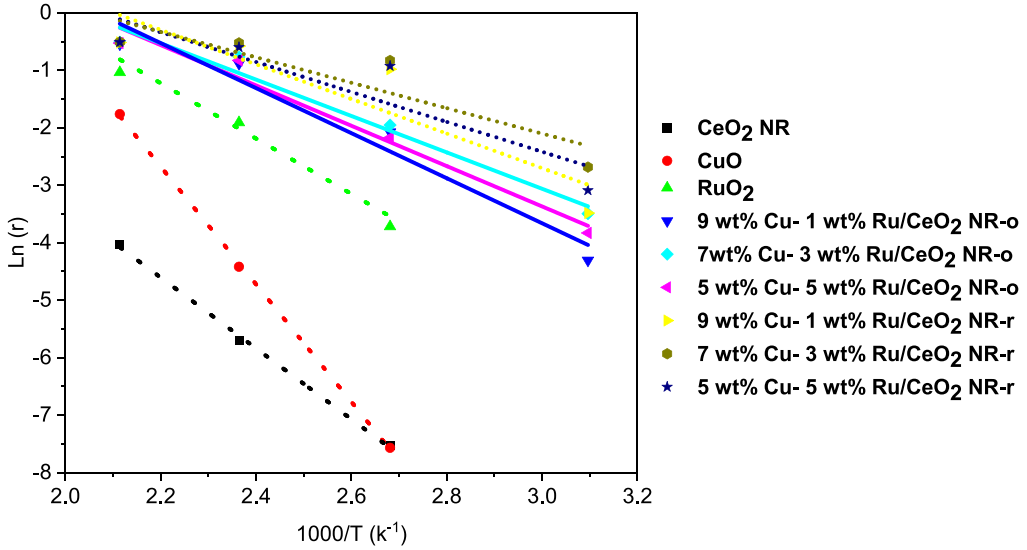

Fig. 13. Arrhenius plots of catalytic CO oxidation over all samples.

Fig. 12 **(a, b)** show the normalized CO conversions for the oxidized and reduced CeO_2 NR-supported CuO_x-RuO_x bimetallic catalysts. For comparison purposes, the CO oxidation performance of CeO_2 NR, CuO, and RuO_2 are included. Clearly, all six CeO_2 NR-supported CuO_x-RuO_x bimetallic catalysts outperform the CeO_2 support and unsupported CuO and RuO_2 catalysts, indicating the promoting role of CeO_2 NR support and/or synergistic effect due to catalyst-support interaction [62,63]. CeO_2 NR, CuO, and RuO_2 showed moderate CO oxidation activity with T_{50} = 315 °C, 220 °C, and 181 °C, respectively, as shown in Table 3. All the oxidized catalysts achieved at least 50 % CO conversion at ~126 °C. Among them, the 7 wt% Cu-3 wt% Ru/CeO_2 NR-o exhibited marginally superior oxidation capability, as measured by the 50 % conversion temperature (T_{50}). Similarly, the CO oxidation activity for T_{100} follows in the order of 7 wt% Cu-3 wt% Ru/CeO_2 NR-o (187 °C) > 9 wt% Cu-1 wt% Ru/CeO_2 NR-o (232 °C) > 5 wt% Cu-5 wt% Ru/CeO_2 NR-o (276 °C). After the reduction treatment, all the reduced catalysts presented better low-temperature CO oxidation activity in comparison to the oxidized catalyst. For example, at 200 °C, all the reduced samples achieved 100 % CO conversion. Following the reduction treatment, the catalyst activity ranking based on the 100 % conversion temperature (T_{100}) is as follows: 7 wt% Cu-3 wt% Ru/CeO_2 NR-r (T_{100} = 166 °C) > 9 wt% Cu-1 wt% Ru/CeO_2 NR-r (T_{100} = 187 °C) > 5 wt% Cu-5 wt% Ru/CeO_2 NR-r (T_{100} = 200 °C).

The Mars-van Krevelen approach has been widely used to explain the CO oxidation pathway over CeO_2 NR-supported metal or metal oxide catalysts, where chemisorbed CO interacts with the surface oxygen of CeO_2 NR and/or metal oxide, leading to the formation of oxygen vacancies. During this process, the lattice oxygen in CeO_2 NR allows the restoration of oxygen vacancy on the surface [64]. According to this mechanism, the adsorbed CO molecules take away surface oxygen, via the desorption of CO_2, resulting in the formation of surface oxygen vacancies. These generated oxygen vacancies can trap oxygen molecules, sustaining the reaction. Thus, the compositional change of metal or metal oxide deposition can influence the catalyst-CeO_2 interaction and CO and O_2 adsorption. For example, from their computational study, Liu et al. [65] reported that Cu sites are oxophilic while X sites favor CO adsorption at Cu-X (X = Pt and Rh for Cu_3Pt_7 and Cu_3Rh_7), while both sites favor oxygen binding in Cu_3Ru_7. In this project, since Cu content is equal to or higher than Ru (Cu_5Ru_5, Cu_7Ru_3, and Cu_9Ru_1) in CeO_2 NR supported CuO_x-RuO_x bimetallic catalysts, both active CO and O_2 adsorption sites are available.

It is important to note that single species (CO or O_2) adsorption will result in lower CO conversion, which was overcome by high Cu content in CuO_x-RuO_x bimetallic catalysts in this study. Based on the CO-TPD data, the 7 wt% Cu-3 wt% Ru/CeO_2 NR-r catalyst exhibited a larger CO adsorption than 9 wt% Cu-1 wt% Ru/CeO_2 NR-r and 5 wt% Cu-5 wt % Ru/CeO_2 NR-r catalyst. A possible explaination for the different CO adsorption and conversion could be due to the balanced adsorption and reaction sites in bimetallic catalysts. In addition, it should also be noted that Cu not only can act as an oxophilic metal, but also Cu^+ or Cu^+/Cu^{2+} promotes the CO oxidation [66]. Table 4 compares the CO oxidation activity between 7 wt% Cu-3 wt% Ru/CeO_2 NR-r catalyst (this work) and similar catalysts from the literature. At 166 °C, the present work attained nearly complete CO conversion, surpassing the performance of the catalysts listed in the table.

Fig. 13 shows the Arrhenius plots for the CO oxidation of all prepared supported catalysts, CuO, RuO_2, and CeO_2 NR support. The slope of the Arrhenius plot between ln(r) versus 1000/T determines the activation energy E_a. According to Fig. 13, the activation energies E_a increase in the following order: 7 wt% Cu-3 wt% Ru/CeO_2 NR-r < 5 wt% Cu-5 wt% Ru/CeO_2 NR-r < 9 wt% Cu-1 wt% Ru/CeO_2 NR-r < 7 wt% Cu-3 wt% Ru/CeO_2 NR-o < 5 wt% Cu-5 wt% Ru/CeO_2 NR-o < 9 wt% Cu-1 wt% Ru/CeO_2 NR-r < RuO_2 < CuO < CeO_2 NR, confirming the superior catalytic performance of the 7 wt% Cu-3 wt% Ru/CeO_2 NR-r catalyst.

4. Conclusion

The goal of this study was to investigate the effect of different Cu: Ru composition ratios (9:1, 7:3, and 5:5) supported by CeO_2 NR on the physiochemical properties and performance of each catalyst for the CO oxidation reaction. Among the investigated catalysts, the 7 wt% Cu-3 wt % Ru/CeO_2 NR-r catalyst exhibited the highest CO oxidation conversion with T_{100} at 166 °C. This superior performance can be attributed to the presence of a larger number of defect sites, such as lattice distortions, oxygen vacancies, Ce^{3+} ions, and strong reducibility properties due to synergistic interaction between CuO_x and RuO_x. The *in situ* DRIFTS spectra clearly showed CO adsorption by 7 wt% Cu-3 wt% Ru/CeO_2 NR-r catalyst, leading to the formation of surface products such as monodentate carbonate (1513), formats (1361), or bi- or tri-carbonates (1058, 1241, and 1290). In addition, the reduction treatment of the catalyst enhanced the formation of more Ru^{n+} ($4 < n < 6$) sites and surface-active oxygen, thereby further enhancing low-temperature CO conversion performance. The reduction of CuO to Cu_2O and subsequently to Cu (CuO → Cu_2O → Cu) also accelerates the conversion of CO. Consequently, optimizing charge and mass transfer of catalysts and strong interaction between catalyst clusters and oxide supports could be

promising strategies to enhance the catalyst activity.

CRediT authorship contribution statement

Md Robayet Ahasan: Investigation, Methodology, Formal analysis, Writing – original draft, Writing – review & editing. **Ruigang Wang:** Conceptualization, Investigation, Methodology, Supervision, Formal analysis, Writing – review & editing, Funding acquisition.

Declaration of Competing Interest

The authors declare that they have no known competing financial interests or personal relationships that could have appeared to influence the work reported in this paper.

Data availability

No data was used for the research described in the article.

Acknowledgment

This project is supported by the grants from the US National Science Foundation (CBET 1856729 and IIP 2044733). The use of electron microscopy facilities at the Alabama Analytical Research Center (AARC) at The University of Alabama is gratefully acknowledged.

References

[1] N.K. Soliman, Factors affecting CO oxidation reaction over nanosized materials: A review, J. Mater. Res. Technol. 8 (2019) 2395–2407.
[2] B. Coq, F. Figueras, Structure–activity relationships in catalysis by metals: some aspects of particle size, bimetallic and supports effects, Coord. Chem. Rev. 178–180 (1998) 1753–1783.
[3] H.Y. Kim, H.M. Lee, G. Henkelman, CO oxidation mechanism on CeO_2-supported Au nanoparticles, J. Am. Chem. Soc. 134 (2012) 1560–1570.
[4] Z. Liu, Y. Lu, M.P. Confer, H. Cui, J. Li, Y. Li, Y. Wang, S.C. Street, E.K. Wujcik, R. Wang, Thermally stable RuO_x–CeO_2 nanofiber catalysts for low-temperature CO oxidation, ACS Appl. Nano Mater. 3 (2020) 8403–8413.
[5] M.R. Ahasan, M.M. Hossain, X. Ding, R. Wang, Non-equilibrium plasma-assisted dry reforming of methane over shape-controlled CeO_2 supported ruthenium catalysts, J. Mater. Chem. A Mater. 11 (2023) 10993–11009.
[6] H. Yan, Z. Liu, S. Yang, X. Yu, T. Liu, Q. Guo, J. Li, R. Wang, Q. Peng, Stable and catalytically active shape-engineered cerium oxide nanorods by controlled doping of aluminum cations, ACS Appl. Mater. Interfaces 12 (2020) 37774–37783.
[7] A. Trovarelli, J. Llorca, Ceria catalysts at nanoscale: how do crystal shapes shape catalysis? ACS Catal. 7 (2017) 4716–4735.
[8] J. Li, Z. Liu, D.A. Cullen, W. Hu, J. Huang, L. Yao, Z. Peng, P. Liao, R. Wang, Distribution and valence state of Ru species on CeO_2 supports: support shape effect and its influence on CO oxidation, ACS Catal. 9 (2019) 11088–11103.
[9] R. Si, M. Flytzani-Stephanopoulos, Shape and crystal-plane effects of nanoscale ceria on the activity of Au-CeO_2 catalysts for the water–gas shift reaction, Angew. Chem. 120 (2008) 2926–2929.
[10] J. Jones, H. Xiong, A.T. DeLaRiva, E.J. Peterson, H. Pham, S.R. Challa, G. Qi, S. Oh, M.H. Wiebenga, X.I.P. Hernández, Thermally stable single-atom platinum-on-ceria catalysts via atom trapping, Science 353 (2016) (1979) 150–154.
[11] C. Pan, D. Zhang, L. Shi, J. Fang, Template-free synthesis, controlled conversion, and CO oxidation properties of CeO2 nanorods; nanotubes, nanowires, and nanocubes, Eur. J. Inorg. Chem. 2008 (2008) 2429–2436.
[12] Y. Lin, Z. Wu, J. Wen, K. Ding, X. Yang, K.R. Poeppelmeier, L.D. Marks, Adhesion and atomic structures of gold on ceria nanostructures: The role of surface structure and oxidation state of ceria supports, Nano Lett. 15 (2015) 5375–5381.
[13] S.A. Mock, S.E. Sharp, T.R. Stoner, M.J. Radetic, E.T. Zell, R. Wang, CeO_2 nanorods-supported transition metal catalysts for CO oxidation, J. Colloid Interface Sci. 466 (2016) 261–267.
[14] L. Liu, A. Corma, Metal catalysts for heterogeneous catalysis: from single atoms to nanoclusters and nanoparticles, Chem. Rev. 118 (2018) 4981–5079.
[15] J. Li, Z. Liu, R. Wang, Support structure and reduction treatment effects on CO oxidation of SiO_2 nanospheres and CeO_2 nanorods supported ruthenium catalysts, J. Colloid Interface Sci. 531 (2018) 204–215.
[16] B. Huang, H. Kobayashi, T. Yamamoto, T. Toriyama, S. Matsumura, Y. Nishida, K. Sato, K. Nagaoka, M. Haneda, W. Xie, A CO adsorption site change induced by copper substitution in a ruthenium catalyst for enhanced CO oxidation activity, Angew. Chem. Int. Ed. 58 (2019) 2230–2235.
[17] T. Mitsui, T. Matsui, R. Kikuchi, K. Eguchi, Low-temperature complete oxidation of ethyl acetate over CeO_2-supported precious metal catalysts, Top. Catal. 52 (2009) 464–469.
[18] K. Mudiyanselage, I. Al-Shankiti, A. Foulis, J. Llorca, H. Idriss, Reactions of ethanol over CeO_2 and Ru/CeO_2 catalysts, Appl Catal B 197 (2016) 198–205.
[19] E. Gonzalez-A, R. Rangel, A. Solís-Garcia, A.M. Venezia, T.A. Zepeda, FTIR investigation under reaction conditions during CO oxidation over Ru(x)-CeO_2 catalysts, Mol. Catal. 493 (2020), 111086.
[20] K. Ebitani, H.-B. Ji, T. Mizugaki, K. Kaneda, Highly active trimetallic Ru/CeO_2/CoO(OH) catalyst for oxidation of alcohols in the presence of molecular oxygen, J. Mol. Catal. A Chem. 212 (2004) 161–170.
[21] V.A. Sadykov, S.F. Tikhov, N.N. Bulgakov, A.P. Gerasev, Catalytic oxidation of CO on CuOx revisited: Impact of the surface state on the apparent kinetic parameters, Catal. Today 144 (2009) 324–333.
[22] G. Wu, N. Guan, L. Li, Low temperature CO oxidation on Cu–Cu_2O/TiO_2 catalyst prepared by photodeposition, Catal, Sci. Technol. 1 (2011) 601–608.
[23] X. Guo, R. Zhou, A new insight into the morphology effect of ceria on CuO/CeO_2 catalysts for CO selective oxidation in hydrogen-rich gas, Catal. Sci. Technol. 6 (2016) 3862–3871.
[24] W.-W. Wang, W.-Z. Yu, P.-P. Du, H. Xu, Z. Jin, R. Si, C. Ma, S. Shi, C.-J. Jia, C.-H. Yan, Crystal Plane effect of ceria on supported copper oxide cluster catalyst for CO oxidation: importance of metal-support interaction, ACS Catal. 7 (2017) 1313–1329.
[25] A. Martínez-Arias, A.B. Hungría, M. Fernández-García, J.C. Conesa, G. Munuera, Interfacial redox processes under CO/O_2 in a nanoceria-supported copper oxide catalyst, J. Phys. Chem. B 108 (2004) 17983–17991.
[26] Y. Guo, J. Lin, C. Li, S. Lu, C. Zhao, Copper manganese oxides supported on multi-walled carbon nanotubes as an efficient catalyst for low temperature CO oxidation, Catal. Lett. 146 (2016) 2364–2375.
[27] M.-L. Lin, M.-Y. Lo, C.-Y. Mou, PtRu nanoparticles supported on ozone-treated mesoporous carbon thin film as highly active anode materials for direct methanol fuel cells, J. Phys. Chem. C 113 (2009) 16158–16168.
[28] J.B. Park, J. Graciani, J. Evans, D. Stacchiola, S.D. Senanayake, L. Barrio, P. Liu, J. F. Sanz, J. Hrbek, J.A. Rodriguez, Gold, copper, and platinum nanoparticles dispersed on CeO_x/TiO_2 (110) surfaces: high water-gas shift activity and the nature of the mixed-metal oxide at the nanometer level, J. Am. Chem. Soc. 132 (2010) 356–363.
[29] D.J. Stacchiola, S.D. Senanayake, P. Liu, J.A. Rodriguez, Fundamental studies of well-defined surfaces of mixed-metal oxides: special properties of $MOx/_{TiO2}$ (110) {M= V, Ru, Ce, or W}, Chem. Rev. 113 (2013) 4373–4390.
[30] M.R. Ahasan, Y. Wang, R. Wang, In situ DRIFTS and CO-TPD studies of CeO_2 and SiO_2 supported CuOx catalysts for CO oxidation, Mol. Catal. 518 (2022), 112085.
[31] R. Wang, R. Dangerfield, Seed-mediated synthesis of shape-controlled CeO_2 nanocrystals, RSC Adv. 4 (2014) 3615–3620.
[32] Z. Wang, Z. Huang, J.T. Brosnahan, S. Zhang, Y. Guo, Y. Guo, L. Wang, Y. Wang, W. Zhan, Ru/CeO_2 catalyst with optimized CeO_2 support morphology and surface facets for propane combustion, Environ. Sci. Tech. 53 (2019) 5349–5358.
[33] S. Tada, H. Nagase, N. Fujiwara, R. Kikuchi, What are the best active sites for CO_2 methanation over Ni/CeO_2? Energy Fuel 35 (2021) 5241–5251.
[34] S.S. Mofarah, E. Adabifiroozjaei, Y. Yao, P. Koshy, S. Lim, R. Webster, X. Liu, R. Khayyam Nekouei, C. Cazorla, Z. Liu, Y. Wang, N. Lambropoulos, C.C. Sorrell, Proton-assisted creation of controllable volumetric oxygen vacancies in ultrathin CeO_{2-x} for pseudocapacitive energy storage applications, Nat. Commun. 10 (2019) 2594.
[35] Z. Liu, J. Li, R. Wang, CeO_2 nanorods supported M-Co bimetallic oxides (M= Fe, Ni, Cu) for catalytic CO and C_3H_8 oxidation, J. Colloid Interface Sci. 560 (2020) 91–102.
[36] Z. Liu, J. Li, M. Buettner, R.V. Ranganathan, M. Uddi, R. Wang, Metal–support interactions in CeO_2-and SiO_2-supported cobalt catalysts: effect of support morphology, reducibility, and interfacial configuration, ACS Appl. Mater. Interfaces 11 (2019) 17035–17049.
[37] B. Lin, Y. Liu, L. Heng, X. Wang, J. Ni, J. Lin, L. Jiang, Morphology effect of ceria on the catalytic performances of Ru/CeO_2 catalysts for ammonia synthesis, Ind. Eng. Chem. Res. 57 (2018) 9127–9135.
[38] Z. Ma, S. Zhao, X. Pei, X. Xiong, B. Hu, New insights into the support morphology-dependent ammonia synthesis activity of Ru/CeO_2 catalysts, Catal. Sci. Technol. 7 (2017) 191–199.
[39] Y. Wang, Z. Liu, M.P. Confer, J. Li, R. Wang, In-situ DRIFTS study of chemically etched CeO_2 nanorods supported transition metal oxide catalysts, Mol. Catal. 509 (2021), 111629.
[40] H. Zou, S. Chen, Z. Liu, W. Lin, Selective CO oxidation over CuO–CeO_2 catalysts doped with transition metal oxides, Powder Technol. 207 (2011) 238–244.
[41] W. Xu, R. Si, S.D. Senanayake, J. Llorca, H. Idriss, D. Stacchiola, J.C. Hanson, J. A. Rodriguez, In situ studies of CeO_2-supported Pt, Ru, and Pt–Ru alloy catalysts for the water–gas shift reaction: Active phases and reaction intermediates, J. Catal. 291 (2012) 117–126.
[42] A.R. Derk, G.M. Moore, S. Sharma, E.W. McFarland, H. Metiu, Catalytic dry reforming of methane on ruthenium-doped ceria and ruthenium supported on ceria, Top. Catal. 57 (2014) 118–124.
[43] D. Gottschalk, E.A. Hinson, A.S. Baird, H.L. Kitts, K.A. Layman, CO adsorption on hydrated Ru/Al_2O_3: influence of pretreatment, J. Phys. Chem. C 114 (2010) 4950–4960.
[44] S. Sharma, Z. Hu, P. Zhang, E.W. McFarland, H. Metiu, CO_2 methanation on Ru-doped ceria, J. Catal. 278 (2011) 297–309.
[45] L. Qi, Q. Yu, Y. Dai, C. Tang, L. Liu, H. Zhang, F. Gao, L. Dong, Y. Chen, Influence of cerium precursors on the structure and reducibility of mesoporous CuO-CeO_2 catalysts for CO oxidation, Appl Catal B 119–120 (2012) 308–320.
[46] J.L. Liu, Z. Li, J.H. Liu, K. Li, H.Y. Lian, X.S. Li, X. Zhu, A.M. Zhu, Warm-plasma catalytic reduction of CO_2 with CH_4, Catal. Today 330 (2019) 54–60.

[47] L. Lin, S. Yao, Z. Liu, F. Zhang, N. Li, D. Vovchok, A. Martínez-Arias, R. Castañeda, J. Lin, S.D. Senanayake, D. Su, D. Ma, J.A. Rodriguez, In situ characterization of Cu/CeO_2 nanocatalysts for CO_2 hydrogenation: morphological effects of nanostructured ceria on the catalytic activity, J. Phys. Chem. C 122 (2018) 12934–12943.
[48] M. Piumetti, S. Bensaid, D. Fino, N. Russo, Nanostructured ceria-zirconia catalysts for CO oxidation: Study on surface properties and reactivity, Appl. Catal. B 197 (2016) 35–46.
[49] H. Zhu, Y. Chen, Z. Wang, W. Liu, L. Wang, Catalytic oxidation of CO over mesoporous copper-doped ceria catalysts via a facile CTAB-assisted synthesis, RSC Adv. 8 (2018) 14888–14897.
[50] W. Jin, Y. Liu, J. Yu, X. Guo, D. Mao, Effect of copper precursors on CO oxidation catalyzed by CuO-CeO_2 prepared by solvothermal method, J. Rare Earths (2022).
[51] X. Hu, D. Mao, J. Yu, Z. Xue, Low-temperature CO oxidation on CuO-CeO_2-ZrO_2 catalysts prepared by a facile surfactant-assisted grinding method, Fuel 340 (2023), 127529.
[52] Y. Liu, D. Mao, J. Yu, X. Guo, Z. Ma, Low-temperature CO oxidation on CuO-CeO_2 catalyst prepared by facile one-step solvothermal synthesis: Improved activity and moisture resistance via optimizing the activation temperature, Fuel 332 (2023), 126196.
[53] W. Shen, D. Mao, Z. Luo, J. Yu, CO oxidation on mesoporous SBA-15 supported CuO–CeO_2 catalyst prepared by a surfactant-assisted impregnation method, RSC Adv. 7 (2017) 27689–27698.
[54] A. Chen, Y. Zhou, N. Ta, Y. Li, W. Shen, Redox properties and catalytic performance of ceria–zirconia nanorods, Catal. Sci. Technol. 5 (2015) 4184–4192.
[55] S.A. Mock, E.T. Zell, S.T. Hossain, R. Wang, Effect of reduction treatment on CO oxidation with CeO_2 nanorod-supported CuOx catalysts, ChemCatChem 10 (2018) 311–319.
[56] S. Galvagno, C. Crisafulli, R. Maggiore, A. Giannetto, J. Schwank, TPR investigation of bimetallic Ru-Cu samples supported on SiO_2, Al_2O_3 and MgO, J. Therm. Anal. 32 (1987) 471–483.
[57] M. Lykaki, S. Stefa, S.A.C. Carabineiro, M.A. Soria, L.M. Madeira, M. Konsolakis, Shape effects of ceria nanoparticles on the water-gas shift performance of CuOx/CeO_2 catalysts, Catalysts 11 (2021) 753.
[58] J. Shi, F. Hui, J. Yuan, Q. Yu, S. Mei, Q. Zhang, J. Li, W. Wang, J. Yang, J. Lu, Ru-Ti oxide based catalysts for HCl oxidation: The favorable oxygen species and influence of Ce additive, Catalysts 9 (2019) 108.
[59] D. Ugur, A.J. Storm, R. Verberk, J.C. Brouwer, W.G. Sloof, Kinetics of reduction of a RuO_2(110) Film on Ru(0001) by H_2, J. Phys. Chem. C 116 (2012) 26822–26828.
[60] X. Liu, Q. Han, W. Shi, C. Zhang, E. Li, T. Zhu, Catalytic oxidation of ethyl acetate over Ru–Cu bimetallic catalysts: Further insights into reaction mechanism via in situ FTIR and DFT studies, J. Catal. 369 (2019) 482–492.
[61] C.H. Wu, C. Liu, D. Su, H.L. Xin, H.-T. Fang, B. Eren, S. Zhang, C.B. Murray, M. B. Salmeron, Bimetallic synergy in cobalt–palladium nanocatalysts for CO oxidation, Nat. Catal. 2 (2019) 78–85.
[62] C. Yang, X. Yu, S. Heißler, A. Nefedov, S. Colussi, J. Llorca, A. Trovarelli, Y. Wang, C. Wöll, Surface faceting and reconstruction of ceria nanoparticles, Angew. Chem. Int. Ed. 56 (2017) 375–379.
[63] G. Spezzati, A.D. Benavidez, A.T. DeLaRiva, Y. Su, J.P. Hofmann, S. Asahina, E. J. Olivier, J.H. Neethling, J.T. Miller, A.K. Datye, CO oxidation by Pd supported on CeO_2 (100) and CeO_2 (111) facets, Appl Catal B 243 (2019) 36–46.
[64] Z. Liu, J. Li, R. Wang, CeO_2 nanorods supported M-Co bimetallic oxides (M = Fe, Ni, Cu) for catalytic CO and C_3H_8 oxidation, J. Colloid Interface Sci. 560 (2020) 91–102.
[65] Y. Liu, H. Li, W. Cen, J. Li, Z. Wang, G. Henkelman, A computational study of supported Cu-based bimetallic nanoclusters for CO oxidation, PCCP 20 (2018) 7508–7513.
[66] A.S. Khder, S.A. Ahmed, H.M. Altass, M. Morad, A.A. Ibrahim, CO oxidation over nobel metals supported on copper oxide: effect of Cu^{+}/Cu^{2+} ratio, J. Mater. Res. Technol. 9 (2020) 14200–14211.
[67] W. Xiao, S. Yang, P. Zhang, P. Li, P. Wu, M. Li, N. Chen, K. Jie, C. Huang, N. Zhang, Facile synthesis of highly porous metal oxides by mechanochemical nanocasting, Chem. Mater. 30 (2018) 2924–2929.
[68] C.S. Chen, T.C. Chen, C.C. Chen, Y.T. Lai, J.H. You, T.M. Chou, C.H. Chen, J.-F. Lee, Effect of Ti_3^{+} on TiO_2-supported Cu catalysts used for CO oxidation, Langmuir 28 (2012) 9996–10006.
[69] A.-P. Jia, S.-Y. Jiang, J.-Q. Lu, M.-F. Luo, Study of catalytic activity at the CuO−CeO_2 interface for CO oxidation, J. Phys. Chem. C 114 (2010) 21605–21610.
[70] J. Cao, Y. Wang, J. Shi, G. Sun, Z. Zhang, Mesoporous CuO/ZrO_2 nanocatalysts: synthesis, characterization and low-temperature CO oxidation activities, J. Porous Mater. 18 (2011) 667–672.
[71] M. Pacella, A. Garbujo, J. Fabro, M. Guiotto, Q. Xin, M.M. Natile, P. Canu, P. Cool, A. Glisenti, PGM-free CuO/$LaCoO_3$ nanocomposites: New opportunities for TWC application, Appl. Catal. B 227 (2018) 446–458.
[72] J.S. Elias, M. Risch, L. Giordano, A.N. Mansour, Y. Shao-Horn, Structure, bonding, and catalytic activity of monodisperse, transition-metal-substituted CeO_2 nanoparticles, J. Am. Chem. Soc. 136 (2014) 17193–17200.